

# An XFEM-based numerical strategy to model three-dimensional fracture propagation regarding crack front segmentation

Fang Shi<sup>a,\*</sup>, Daobing Wang<sup>b</sup>, Quanquan Yang<sup>a</sup>

<sup>a</sup> Jiangsu Key Laboratory of Advanced Manufacturing Technology, Huaiyin Institute of Technology, Huai'an Jiangsu, 223003, China

<sup>b</sup> School of Mechanical Engineering, Beijing Key Laboratory of Pipeline Critical Technology and Equipment for Deep Water Oil & Gas Development, Beijing Institute of Petrochemical Technology, Beijing 102617, China

## ARTICLE INFO

### Keywords:

XFEM  
Crack front segmentation  
Echelon crack  
Mixed-mode fracture  
Fluid-driven fracture

## ABSTRACT

Under mixed I-III loading, a crack frequently segments into several echelon-shaped daughter cracks rotated towards the direction of principal stress. This phenomenon is called crack front segmentation and has been widely observed at different length scales in both laboratory and nature. In this paper, based on the extended finite element method (XFEM), a three-dimensional numerical strategy is proposed, validated, and adopted to model quasi-static fracture propagation considering crack front segmentation. A new crack propagation criterion based on the weighted average principal stress in conjunction with a cubic spline curve fitting of front vertexes is introduced to update the crack geometry. Further, to get a higher resolution of the stress field around the crack front, a robust and efficient local mesh refinement scheme fully integrated with the XFEM is proposed. Besides, a partitioning scheme of enriched elements containing segmentation points is presented to achieve an accurate numerical integration. Several examples are presented to illustrate the effectiveness and robustness of the proposed strategy. The hydraulic fracturing example indicates that ignoring fracture front segmentation for a mixed-mode I-III fluid-driven fracture will severely underestimate the injection pressure due to the stress shadow effects between adjacent overlapped segments.

## 1. Introduction

It has been well-known that, except under special circumstances, the crack front grows towards mode-I loading conditions no matter what the external loading is [1]. Under mixed-mode I-II loading conditions, the crack front kinks or curves to eliminate mode-II. Under mixed-mode I-III or I-II-III loading conditions, however, the problem turns to three-dimensional (3D), and the crack front twists and generally splits into an array of segments (as depicted in Fig. 1), and eventually achieves pure mode-I situations for each segment. This phenomenon is known as crack front segmentation [2–4] or crack front fragmentation [5,6], and the oriented segments are termed echelon cracks [5–7] or tilted facets [8–10]. Starting from the seminal works of Sommer [11] and Knauss [12], crack front segmentation has been observed at different length scales from millimeter [1] to kilometer [2,7] in both laboratory and nature [13] in various materials such as rocks [7,13–16], glass [11], polymers [1,9,12,17], metals [3], and jel [18], as typically shown in Fig. 2. This implies that the causes of segmentation are material-independent and size-independent. Hence, the classical linear elastic

fracture mechanics (LEFM) in macroscale is capable of dealing with such problems [2,9,19]. The phenomenon of crack front segmentation is very complex. Experiments show that the occurrence of segmentation is related to the ratio of mode-III ( $K_{III}$ ) to mode-I ( $K_I$ ) stress intensity factors (SIFs) [19] and some threshold values are proposed [10]. Yet in some other experiments [18,20], even an extremely low ratio of mode mixture can trigger segmentation. Besides, both experiments and phase-field simulation show that crack coarsening [9,21,22] happens during the further propagation process of echelon cracks, which further complicates the problem. Fortunately, it has been observed in experiments [11,13,23,24] that the initially generated echelon cracks are in a perfectly periodic pattern, oriented with similar angles, separated by nearly an equal distance, and have almost the same size, just as illustrated in Fig. 1.

Some theoretical work has been done to decipher when and how segmentation occurs in materials under mixed-mode loadings. For example, Cooke and Pollard [17] presented a simple model to determine the twist angle by assuming that the echelon crack grows within a plane perpendicular to the maximum principal stress. Lazarus et al. proposed a

\* Corresponding author.

E-mail address: [shifang@hyit.edu.cn](mailto:shifang@hyit.edu.cn) (F. Shi).

<https://doi.org/10.1016/j.tafmec.2022.103250>

Received 8 December 2021; Received in revised form 4 January 2022; Accepted 4 January 2022

Available online 10 January 2022

0167-8442/© 2022 Elsevier Ltd. All rights reserved.

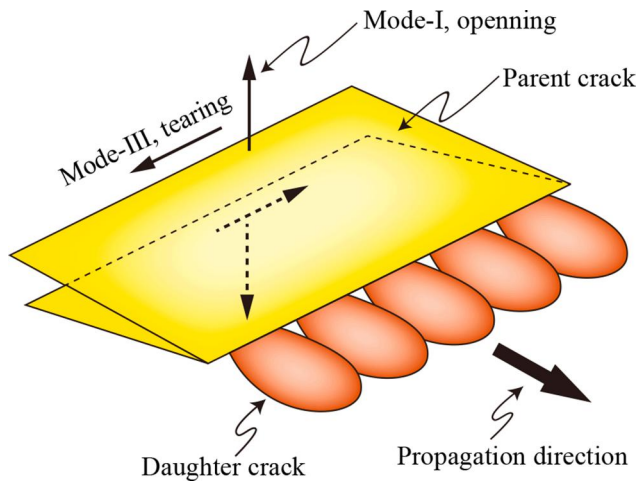


**Fig. 1.** Illustration of the segmented crack front under the action of mixed-mode I-III loading conditions. Five daughter cracks (or called echelon cracks or crack segments) parallel to each other were formed from the front of the flat parent crack and rotated towards the direction of principal stress [2].

model [25] to theoretically calculate SIFs along the crack front after growth over a small distance and established a criterion [26] to predict the crack front rotation rate. Lazarus et al. [1] then compared crack propagation paths predicted by several propagation criteria with experimental results. Wu et al. [22] established a 2D theoretical model to investigate the influence of interaction between adjacent echelon cracks based on observation of experimental results. Lin et al. [5] proposed a crack front segmentation criterion and a theoretical model linking the fragment spacing and the twist angle. Within the framework of LEFM, Leblond et al. [27] derived the expressions of SIFs along the segmented crack front described by helices. Leblond and Frelat [28] deduced an expression of the twist angle over the ratio of  $K_{III}$  to  $K_I$  after analytically obtaining solutions of a two-dimensional (2D) problem that

contains an array of inclined cracks in an infinite plate under uniform loading at infinity. Although some achievements have been reached, it should be noted that a constant picture between theoretical predictions and experimental results has not been obtained yet [9]. Therefore, researchers need to resort to numerical methods to deal efficiently with this kind of intricate problems.

It is now well-known that, in practice, most 3D fracture problems in engineering are in mixed mode, and crack front segmentation constantly occurs as depicted in Fig. 2. However, due to the extreme complexity, researchers usually assume the integrality of the 3D crack surface and ignore the segmentation process of crack front in their numerical models [29–32], thus, to some extent, resulting in inaccurate or even unreliable simulation results. When it comes to the numerical simulation of problems concerning segmented crack front, the most widely used approach in recent years is the phase-field method [33]. For example, based on the phase-field method, Pons and Karma [21] observed that facets will gradually coarsen (i.e., facet coarsening) during crack-front evolution through large-scale simulations of mixed-mode fracture. Chen et al. [9] studied in detail the facet coarsening process by performing phase-field simulations, and found facet coarsening is driven by the instability of spatial period-doubling of facets during propagation. Henry [34] showed that irregular initial slits can result in front segmentation even for very small  $K_{III}/K_I$  ratios as observed in experiments [22]. Pham and Ravi-Chandar [6] proposed a phase-field model of fracture and suggested the introduction of initial defects around crack front to trigger the occurrence of crack front segmentation. However, although automatic tracking of crack front evolution with arbitrary complex geometries is a particularly attractive advantage of the phase-field method, an inherent drawback of this method limits its application to research purposes only, rather than practical engineering problems. As a key parameter in the phase-field method, the intrinsic length scale must be taken small enough [6] compared to the scale of echelon cracks in order to correctly capture the crack front segmentation process. As a result, the computational domain contains a huge number of elements or grid points (for example, millions of elements in [6] and up to  $10^8$  grid points in [21]) even for a microscale simulation that can only be performed using large-

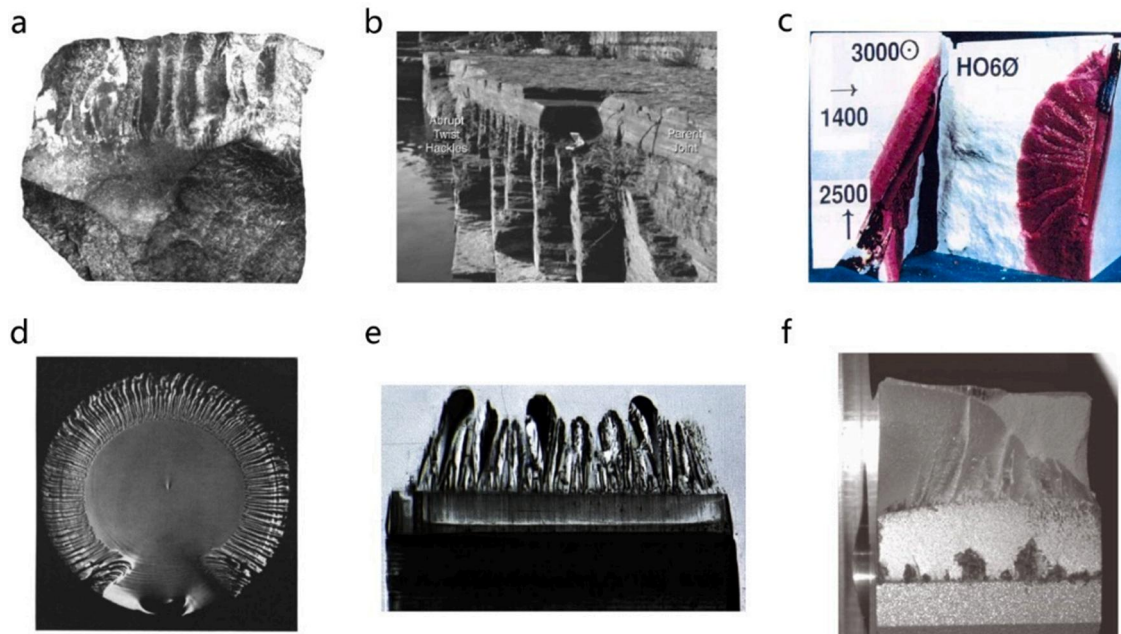


**Fig. 2.** Crack front segmentation phenomenon observed in nature ((a) and (b)) and in laboratory ((c) - (f)). (a) Echelon cracks (upper part of the figure) and the parent crack (lower part of the figure) observed in a shale specimen [7]. (b) Natural echelon cracks photographed at Taughannock Falls State Park [13]. (c) Segmented hydraulic fracture formed from a horizontal wellbore in a block of hydrostone [14]. (d) Lance-shaped facets produced around the crack front of a cylindrical bar made of glass loaded in both tension and a tiny amount of torsion [11]. (e) Facets observed in three points bending experiment of a plexiglass beam [9]. (f) Fractured surface of a CTSR (Compact Tension Shear Rotation)-specimen made of high-strength aluminium alloy [3].

scale parallel computers [21].

In addition to the phase-field method, Huang et al. [35] reproduced the crack front segmentation phenomenon in 3D hydraulic fracture propagation simulations performed using the virtual internal bond (VIB) method. Meng and Pollard [36] modeled 3D crack propagation process in mixed-mode based on the boundary element method (BEM) and compared the crack surface evolutions with and without considering segmented crack front. Leblond and Lazarus et al. [10] proposed a multiscale cohesive-zone model derived in the context of LFEM by assuming that facet length is much bigger than its spacing. Recently, Lazarus et al. [8,37] improved their cohesive-zone model to handle more realistic cases and investigated toughening caused by facets. The finite element method (FEM) shows great flexibility in a variety of complicated problems. However, the FEM is not a versatile method to investigate the crack front fragmentation phenomenon in which the tip-line twists and fragments into echelon cracks (as shown in Fig. 1) due to the difficulty in meshing around the complex geometries. For example, Xu et al. [38] predicted unstable out-of-plane propagation under combined mode I-III loading conditions using the FEM, but their model is incapable of allowing the crack front line to break into segments. In addition, Dhondt et al. [39] and Buchholz et al. [40] numerically analyzed three-point bending experiments of polymethyl methacrylate (PMMA) under mixed-mode loading conditions with no regard to fragmentation. More recently, Thomas et al. [32] simulated mixed-mode growth of fractures in arrays and networks using FEM, but also without considering crack front segmentation.

The XFEM [41–43] was proposed by enriching the displacement-based approximation with additional basis functions and enriched degrees of freedom (DOFs) based on the partition of unity method [44]. Using the XFEM, the task of tedious remeshing of finite element mesh can be completely avoided, and thus it shows excellent applicability and high flexibility for a variety of practical problems in both 2D and 3D [30,45,46]. It must be mentioned that, within the framework of XFEM, the local mesh refinement can be performed in the vicinity of the crack to further improve the resolution of stress field. For example, Wang et al. [47] proposed a local mesh refinement scheme with variable-node transition hexahedral elements through which the mismatching element interfaces between different meshes can directly be converted into matching interfaces. It should be noted that a similar numerical approach based on the partition of unity theory, the generalized finite element method (GFEM) [46], has also been used as a versatile tool to study problems involving cracks of complex geometry. Pereira et al. [48] proposed a GFEM-based model and investigated the effects of mode-III SIF on crack propagation paths. They [48] found that a desired mode-I planar crack growth status cannot be reached at the end of a simulation if neglecting mode-III effects in the adopted crack propagation criterion. Gupta and Duarte [29] studied the 3D non-planar and non-smooth propagation of fluid-driven cracks with a focus on the influence of in-situ stresses and pumping pressure on crack shape evolution using adaptive GFEM. Recently, Shi and Liu [30] proposed a fully-coupled model to investigate the hydraulic fracturing procedure of 3D non-planar fractures based on the XFEM and observed that mode-III SIF has a profound effect on crack propagation paths. In their study [30], Schöllmann’s criterion is adopted as the crack propagation criterion and they discussed the importance of fracture front segmentation in hydraulic fracturing simulation. Xiao et al. [49] established a numerical model in which the crack is explicitly described by a B-spline ruled surface to simulate arbitrary 3D crack propagation in the framework of XFEM. Besides, Mukhtar et al. [50] studied mixed-mode fracture propagation in brittle materials using GFEM/XFEM in conjunction with the mesh adaptivity technique. Although some scholars have tried to investigate non-planar crack propagation problems under mixed loading conditions using the XFEM or GFEM, to our knowledge, relevant research that explicitly considers crack front segmentation has not been reported in the literature yet.

The paper is arranged as follows. Methodology including a brief

description of the XFEM and the crack propagation criterion are given in Section 2. Section 3 details modeling hypotheses and some implementation issues. Verification of the proposed numerical strategy and numerical examples including hydraulic fracturing simulation are presented in Section 4, followed by concluding remarks in Section 5. In this paper, we try for the first time to offer an XFEM-based numerical strategy to simulate echelon cracks formation while twisting along the crack front line. To efficiently achieve this objective, a new weighted average principal stress criterion (Section 2.2) along with a local mesh refinement algorithm (Section 3.1) and a curve fitting method of crack front vertexes (Section 3.2) is proposed. Besides, a scheme of partitioning enriched elements containing segmentation points to achieve an accurate numerical integration is presented in Section 3.3.

## 2. Methodology

### 2.1. XFEM in linear elastic fracture mechanics

Consider a 3D quasi-static crack inside a linear-elastic domain  $\Omega$  with boundary  $\Gamma$  which is composed of four non-overlapping regions:  $\Gamma_u$  with imposed displacement  $\bar{\mathbf{u}}$ ,  $\Gamma_t$  with externally enforced stress  $\mathbf{t}$ , the crack surface  $\Gamma_c$  composed of  $\Gamma_c^+$  and  $\Gamma_c^-$ , and the rest region of  $\Gamma$ . Neglect body forces, the equilibrium equation and corresponding boundary conditions read

$$\begin{cases} \nabla \cdot \boldsymbol{\sigma} = 0 & \text{in } \Omega \\ \mathbf{u} = \bar{\mathbf{u}} & \text{on } \Gamma_u \\ \boldsymbol{\sigma} \cdot \mathbf{n}_{\Gamma_t} = \mathbf{t} & \text{on } \Gamma_t \\ \boldsymbol{\sigma} \cdot \mathbf{n}_{\Gamma_c} = P \mathbf{n}_{\Gamma_c} & \text{on } \Gamma_c \end{cases} \quad (1)$$

where  $\mathbf{n}_{\Gamma_t}$  and  $\mathbf{n}_{\Gamma_c}$  represent the outwards normal vectors of boundary  $\Gamma_t$  and  $\Gamma_c$ , respectively;  $\boldsymbol{\sigma}$  denotes the Cauchy stress tensor and is computed as

$$\boldsymbol{\sigma} = \mathbf{D} : \boldsymbol{\varepsilon} \quad (2)$$

In this equation,  $\mathbf{D}$  represents the elasticity matrix of moduli, and  $\boldsymbol{\varepsilon}$  is the strain tensor under small deformation theory assumptions. In Eq. (1),  $P$  denotes the fluid pressure inside the crack for the hydraulic fracturing simulation performed in Section 4.5; in other simulations,  $P$  equals 0.

After finite element discretization of the domain  $\Omega$ , we obtain:  $S_{all}$ , the set of all nodes;  $S_{frac}$ , the set of nodes attached to elements completely cut by the crack surface (also known as Heaviside enriched nodes); and  $S_{tip}$ , the set of nodes attached to elements intersected by crack front. Then, the displacement  $\mathbf{u}$  of point  $\mathbf{x}$  in  $\Omega$  can be calculated by [43]

$$\mathbf{u}(\mathbf{x}) = \sum_{I \in S_{all}} N_I^u(\mathbf{x}) \mathbf{u}_I + \sum_{I \in S_{frac}} N_I^u(\mathbf{x}) H(\mathbf{x}) \mathbf{a}_I + \sum_{I \in S_{tip}} N_I^u(\mathbf{x}) \sum_{l=1}^4 F_l(\mathbf{x}) \mathbf{b}_I^l \quad (3)$$

In the above,  $\mathbf{u}_I$  is the vector of conventional displacement DOFs,  $\mathbf{a}_I$  and  $\mathbf{b}_I^l$  are vectors of additional displacement DOFs of node sets  $S_{frac}$  and  $S_{tip}$ , respectively.  $N_I^u$  is the classical  $C^0$  shape function.  $H(\mathbf{x})$  represents the Heaviside enrichment function and

$$H(\mathbf{x}) = \begin{cases} 1 & \text{if } (\mathbf{x} - \mathbf{x}^*) \cdot \mathbf{n}_{\Gamma_c} \geq 0 \\ -1 & \text{otherwise} \end{cases} \quad (4)$$

where  $\mathbf{x}^*$  denotes the nearest point on  $\Gamma_c$  to  $\mathbf{x}$ . Besides,  $F_l(\mathbf{x})$  denote the tip enrichment functions (or branch functions). Define a local Cartesian coordinate system represented by  $(x, y, z)$  and a local cylindrical coordinate system represented by  $(r, \theta, z)$  along the crack front, as shown in Fig. 3. Both coordinate systems originate from the midpoint  $\mathbf{x}'$  of each crack front line segment and share the same  $z$ -axis defined along the crack front line segment. Besides, the  $y$ -axis coincides with  $\mathbf{n}_{\Gamma_c}$ . Subsequently,  $F_l(\mathbf{x})$  can be expressed as [43]:

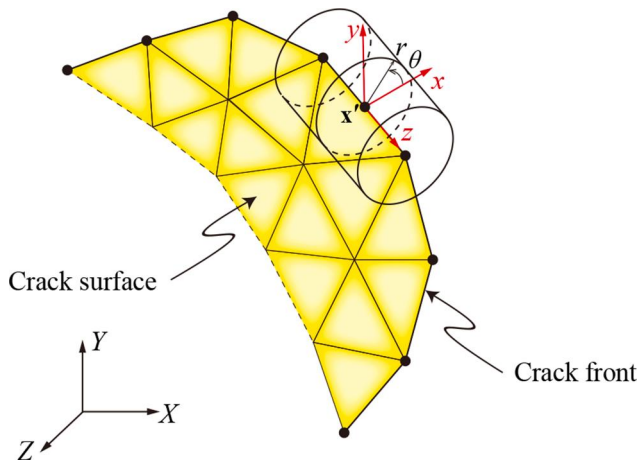


Fig. 3. Illustration of the local Cartesian coordinate system represented by  $(x, y, z)$  and the cylindrical coordinate system represented by  $(r, \theta, z)$  defined along the crack front. Crack surface is represented by spatial triangular patches in an explicit manner [30].

$$\{F_l(r, \theta)\}_{l=1, \dots, 4} = \left\{ \sqrt{r} \sin \frac{\theta}{2}, \sqrt{r} \cos \frac{\theta}{2}, \sqrt{r} \sin \theta \sin \frac{\theta}{2}, \sqrt{r} \sin \theta \cos \frac{\theta}{2} \right\} \quad (5)$$

For the blending elements (or called partially enriched elements) [51], which are constructed between the enriched and standard elements, the partition of unity [44] does not hold. To solve this problem, an effective and simple approach proposed by Fries [52] is adopted in this study. For the enrichment function  $\psi(\mathbf{x})$  of enriched node set  $S_{enrich}$ , define the modified enrichment function  $\psi^{mod}(\mathbf{x})$  as [52]

$$\psi^{mod}(\mathbf{x}) = \psi(\mathbf{x})R(\mathbf{x}) \quad (6)$$

where  $R(\mathbf{x})$  represents a linearly decreasing weight function called ramp function:

$$R(\mathbf{x}) = \sum_{I \in S_{enrich}} N_I^u(\mathbf{x}) \quad (7)$$

Then, Eq. (3) can be rewritten as

$$\mathbf{u}(\mathbf{x}) = \sum_{I \in S_{all}} N_I^u(\mathbf{x}) \mathbf{u}_I + \sum_{\alpha=1}^{NE} \sum_{I \in M_{enrich}} N_I^u(\mathbf{x}) \psi_\alpha^{mod}(\mathbf{x}) \mathbf{c}_I^\alpha \quad (8)$$

where  $M_{enrich}$  denotes the set of all enriched nodes and all other nodes of blending elements,  $NE$  represents the number of enrichment functions, and  $\mathbf{c}_I$  represents the vector of additional displacement DOFs of corresponding enrichment function.

In the literature, the geometrical enrichment approach [53] is often used to select the tip-enriched nodes in order to gain better convergence rates [54]. According to this approach, nodes located inside the sphere centered at the crack front vertex are all taken as tip-enriched nodes. As an alternative, in this study, a new approach based on local mesh refinement is proposed and the performance comparison of both approaches will be presented in Section 4.1.

The weak form of Eq. (1) can be obtained by introducing the test function  $\delta \mathbf{u}(\mathbf{x}, t)$

$$\int_{\Omega} \delta \boldsymbol{\varepsilon} : \boldsymbol{\sigma} d\Omega + \int_{\Gamma_c} [[\delta \mathbf{u}]] \cdot \mathbf{P} \mathbf{n}_{\Gamma_c} d\Gamma = \int_{\Gamma_i} \delta \mathbf{u} \cdot \mathbf{t} d\Gamma \quad (9)$$

where  $[[\delta \mathbf{u}]] = \delta \mathbf{u}(\Gamma_c^+) - \delta \mathbf{u}(\Gamma_c^-)$  denotes the displacement jump across  $\Gamma_c$ . Afterwards, the discretization form of equilibrium equation can then be derived by substituting Eqs. (2) and (3) to its weak form:

$$\mathbf{K} \mathbf{U} - \mathbf{Q} \mathbf{P} - \mathbf{F} = \mathbf{0} \quad (10)$$

In the above equation,  $\mathbf{K}$ ,  $\mathbf{U}$ ,  $\mathbf{F}$ ,  $\mathbf{P}$ , and  $\mathbf{Q}$  represent respectively the

global stiffness matrix, the global displacement vector of conventional DOFs and enriched DOFs, the external force vector, the fluid pressure vector, and the fluid-solid coupling matrix which can be written as

$$\mathbf{Q} = \int_{\Gamma_c} (\mathbf{N}^w)^T \mathbf{n}_{\Gamma_c} \mathbf{N}^p d\Gamma \quad (11)$$

where  $\mathbf{N}^w$  represents the shape function matrix that transfers  $\mathbf{U}$  to crack aperture vector  $\mathbf{w}$ ,  $\mathbf{N}^p$  represents the shape function matrix of fluid pressure elements [30].

## 2.2. Crack propagation criterion

The crack propagation criterion is one of the most important components of a numerical model to simulate the fracture propagation process. Generally, a quasi-static crack propagation criterion is composed of three parts, i.e., whether a crack front vertex grows or not, along which direction if it grows, and how far it grows. Schöllmann's criterion, which is an extension of the 2D maximum tangential stress criterion (MTS) to 3D [1], has been adopted by many researchers [1,30,31,48]. This criterion depends on the calculation of SIFs, and details can be seen in our recent work [30]. However, it has been found that the high accuracy of SIFs obtained in 2D XFEM problems cannot be easily repeated in 3D XFEM problems [49] due to the geometrical complexity of 3D cracks. The displacements and stress fields agree well with the analytical solutions whereas the error of SIFs obtained in 3D problems can be ten times worse [55,56] than that in 2D problems. Besides, researchers show that the SIF-based criterion is not suitable for real formation rock stress conditions [57]. Thus, as an alternative, criteria based directly on the stress field, rather than SIFs, have been widely used [4,5,36,58,59] to perform simulation under mixed loading conditions. Doitrand and Leguillon [4] show that the twist angle of the segment can be determined as the one which maximizes the tensile stress ahead of the parent crack front. Similarly, Wu [22] and Lin et al. [5] conclude that the maximum principal stress criterion (MPSC) is an ideal choice for the simulation of daughter crack growth. This conclusion has also been evidenced by experiments performed by Mittelman and Yosibash [60,61]. Therefore, in this paper, a criterion based on the weighted average principal stress together with a novel weight function is proposed to determine when and how the crack propagates.

Since the vertexes of the crack front are rarely located at the Gauss points, when calculating the stress tensor at a vertex, a non-local one computed as weighted average stress of Gauss points inside a calculation sphere is a more natural choice [62]. The weighted average stress tensor  $\boldsymbol{\sigma}$  is calculated according to

$$\boldsymbol{\sigma} = \sum_{i=1}^{ng} \boldsymbol{\sigma}_i w_i / \sum_{i=1}^{ng} w_i \quad (12)$$

where  $ng$  represents the number of Gauss points inside the calculation sphere centered at the crack front vertex,  $\boldsymbol{\sigma}_i$  represents the stress tensor at Gauss point  $i$ ,  $w_i$  denotes the weight of Gauss point  $i$ , and in this paper:

$$w_i = \left[ 1 - \left( \frac{l_i}{r} \right)^\chi \right]^3 \quad (13)$$

In the above weight function,  $l_i$  represents the distance of Gauss point  $i$  to crack front vertex,  $r$  is the radius of the calculation sphere and is taken as the characteristic element size ( $l_c$ ) of enriched elements (in this paper,  $l_c = \bar{V}_{enr}^{1/3}$  where  $\bar{V}_{enr}$  denotes the average volume of all enriched elements), and parameter  $\chi$  controls the decay speed of the weight function away from the sphere center. Plots of weight functions with different values of  $\chi$  are given in Fig. 4. It can be stated that the stress tensor degrades into a local one when  $\chi$  is close to zero, whereas the stress tensor approaches to an average value with the increase of  $\chi$ , indicating that the parameter  $\chi$  possesses a clear physical meaning. The influence of parameter  $\chi$  on crack propagation paths will be studied in

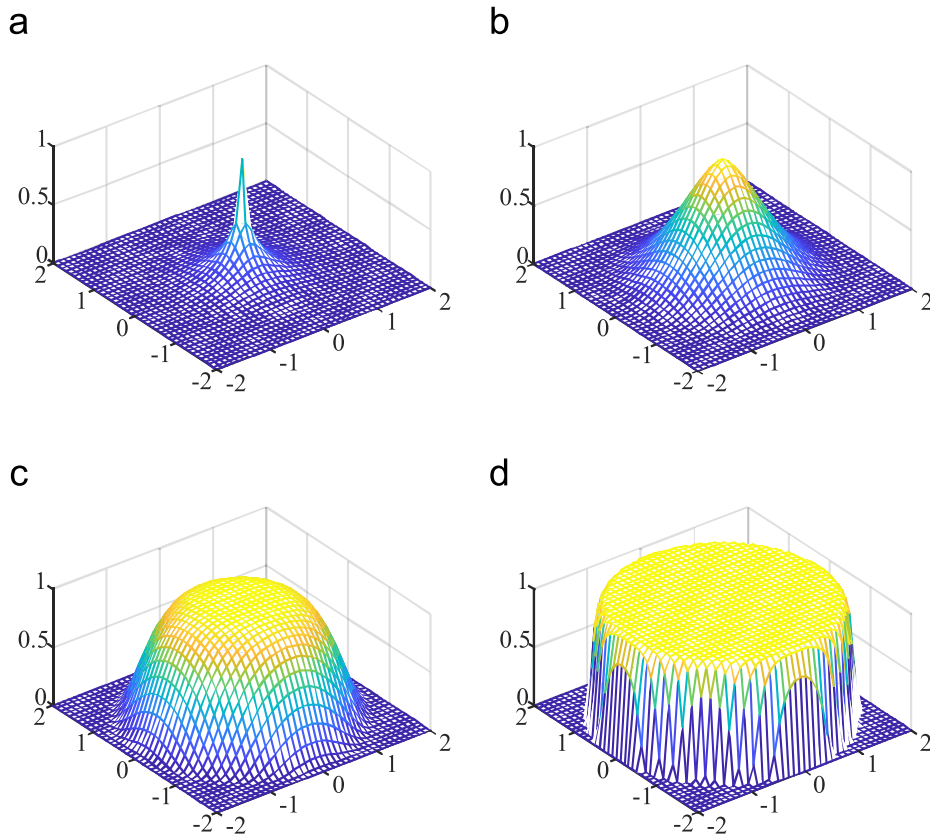


Fig. 4. Plots of weight functions with different values of  $\chi$ . (a)  $\chi = 0.5$ , (b)  $\chi = 1.5$ , (c)  $\chi = 5$ , and (d)  $\chi = 50$ .

Section 4.2.

We assume a linear relationship between the magnitude of crack propagation and the maximum principal stress. Then if the maximum principal stress  $\sigma_1^i$  is larger than the tensile strength  $s_t$ , the propagation vector  $\mathbf{p}_i$  of vertex  $i$  can be obtained as

$$\mathbf{p}_i = \Delta a_{max} \frac{\sigma_1^i}{\bar{\sigma}_1} \mathbf{n}_r^i \tag{14}$$

where  $\Delta a_{max}$  is the model parameter,  $\mathbf{n}_r^i$  is the radial vector of the crack front curve  $s$  at vertex  $i$  and is perpendicular to the direction of principal stress, and  $\bar{\sigma}_1$  represents the average principal stress:

$$\bar{\sigma}_1 = \frac{\oint \sigma_1 ds}{\oint ds} \tag{15}$$

Finally, the coordinates of updated vertex  $i$  can be written as  $\tilde{\mathbf{v}}_i = \mathbf{v}_i + \mathbf{p}_i$ . It should be noted that if the distance between two adjacent vertexes (for example,  $\tilde{\mathbf{v}}_i$  and  $\tilde{\mathbf{v}}_{i+1}$ ) is larger than  $1.5 l_c$ , a new vertex should be added at  $(\tilde{\mathbf{v}}_i + \tilde{\mathbf{v}}_{i+1})/2$ .

To further improve the accuracy and robustness of the proposed propagation criterion, a local mesh refinement algorithm and a cubic spline curve fitting technique are developed and will be described in the next Sections 3.1 and 3.2, respectively.

3. Implementation issues

This section focuses on some implementation issues of the presented numerical strategy. Before continuing, some assumptions are made. Experiments show that in some cases second-order segments emerge on the front of daughter cracks [22]. Here we only consider the first-order segments formed from the parent crack front. Facet coarsening caused by neighboring facets merging [9] is beyond the scope of this paper. That means the segments are not connected with each other. Besides, the

segment length or the total number of segments along the crack front is specified directly in this paper, because segment length is closely related to material parameters, loading conditions, as well as crack size and shape in a complex manner, and is very difficult to be accurately predicted [6,20,63].

3.1. Local mesh refinement algorithm

In this paper, hexahedral elements with 8 nodes are adopted to discretize the 3D computational domain. Due to the inherent complexity of the segmentation process, the stress field of high resolution must be appropriately obtained before deciding the direction and length of crack propagation, which is of particular importance for the crack front segmentation simulation. To fulfill this need, a novel refinement algorithm that can be fully and naturally integrated with the XFEM is proposed to improve the resolution of the stress field along the crack front, especially around the segmentation points. The proposed algorithm only applies refinement to enriched elements with tip-enriched nodes, hence the number of increased DOFs is limited, and most importantly, it can significantly improve the simulation accuracy, as will be shown in Section 4.2. Another merit of local mesh refinement is that the possible inconformity [41] between Heaviside enrichment and tip enrichment of Gauss points in enriched elements that contain kinking crack surface can be completely avoided. Moreover, this algorithm can be easily implemented in XFEM-based codes. A versatile code written in Fortran to perform the algorithm described in this section has been deposited in GitHub and can be accessed from [https://github.com/PhiPsi-Software/local\\_mesh\\_refinement.git](https://github.com/PhiPsi-Software/local_mesh_refinement.git).

For an enriched 8-noded hexahedral element, there are 21 possible configurations of enriched nodes, as depicted in Fig. 5. The red, green, blue, and black elements are subdivided according to refinement templates (a), (b), (c), and (d) shown in Fig. 6, respectively. Refinement templates (a) to (d) contain 4, 11, 22, and 27 refined elements,

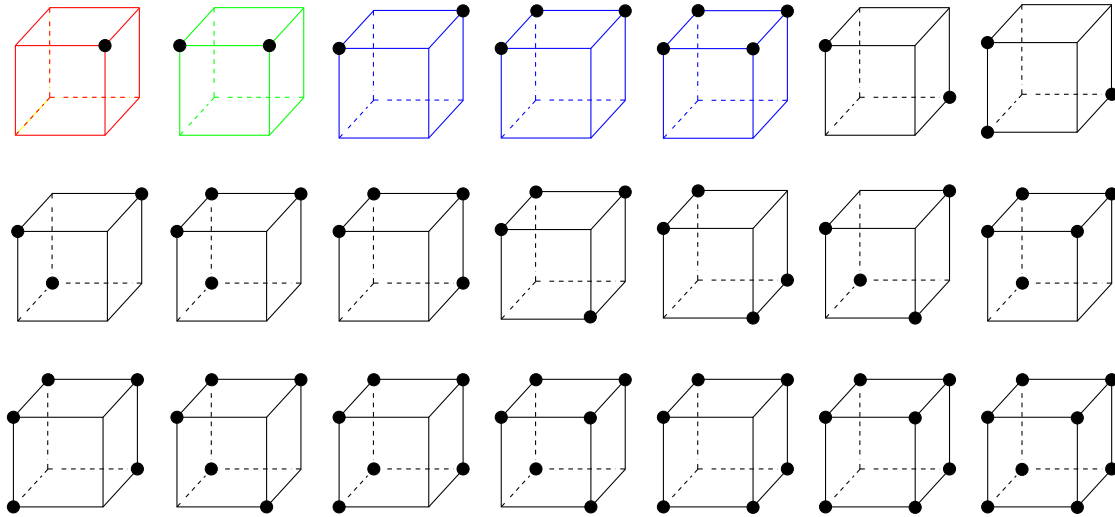


Fig. 5. Enriched elements with different configurations of enriched nodes. The black dots represent enriched nodes.

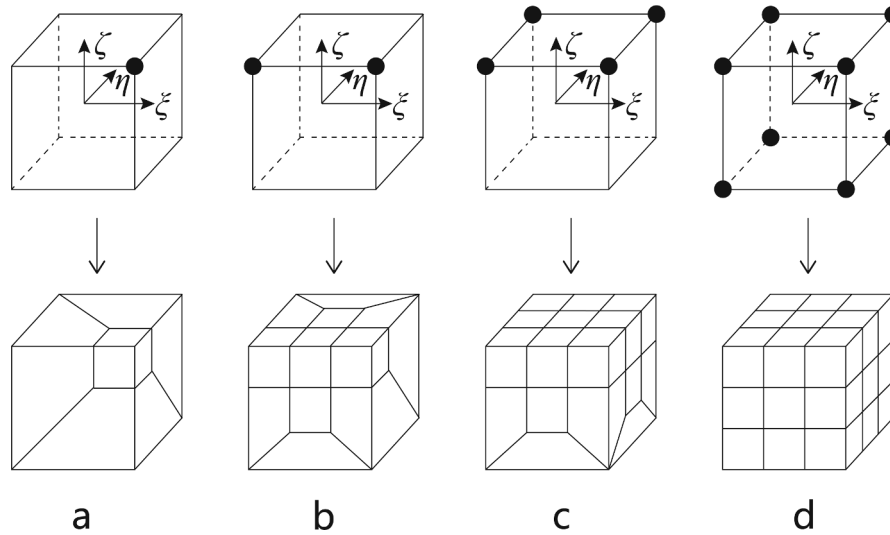


Fig. 6. Refinement templates for elements with different numbers of enriched nodes. The black dots represent enriched nodes.  $(\xi, \eta, \zeta)$  represents the natural coordinate system of enriched elements before refinement. Rules followed by each template are: element edge with one enriched node are split into two edges by adding one node, and element edge with two enriched nodes are split into three edges by adding two nodes.

respectively. Following this strategy, the conformity [64,65] of meshes can be assured, which means, two adjacent elements share the same nodes on both faces and edges.

Subdivision of refinement templates (a) and (d) are straightforward. More attention should be paid to templates (b) and (c). Subdivision details of refinement template (c) are given in Fig. 7 in which the natural coordinates of the inserted nodes 1 to 8 are taken as  $(-1/3, -1, -1/2)$ ,  $(1/3, -1, -1/2)$ ,  $(1/3, 1, -1/2)$ ,  $(-1/3, 1, -1/2)$ ,  $(-1/3, -1/3, 0)$ ,  $(1/3, -1/3, 0)$ ,  $(1/3, 1/3, 0)$ , and  $(-1/3, 1/3, 0)$ , respectively. Hence, it can be easily proved that the colored resulting faces shown in Fig. 7 are all planar. In other words, each colored face has four coplanar nodes, including three inserted nodes and one pre-existing node. As a result, all refined elements, including colored ones shown in Fig. 8, are all hexahedral elements. An important issue needed to be addressed is that when numbering the inserted nodes to newly form a hexahedral element, the determinant of the Jacobian must be ensured to be positive; detailed implementation can be found in our Fortran code deposited in GitHub. Following a similar way, the natural coordinates of the inserted

nodes of refinement template (b) can be determined.

### 3.2. Cubic spline curve fitting of crack front vertexes

Due to the complexity of crack front segmentation, it is favorable to improve the geometrical smoothness of the crack surface after each propagation step. In this study, a smooth representation of the crack surface is obtained by performing cubic spline curve fitting of crack front vertexes using the cubic smoothing spline algorithm [66]. As shown in Fig. 9, for a set of crack front vertexes  $v_i$  ( $i = 1, 2, \dots, n$ ) starts and ends at the segmentation points, the smoothing cubic spline  $f$  minimizes

$$p \sum_{i=1}^n \hat{w}_i |v_i - f(t)|^2 + (1 - p) \int \lambda(t) |D^2 f(t)|^2 dt \tag{16}$$

where the first and second terms are for error measure and roughness measure, respectively. In the above equation,  $t$  denotes the curvilinear

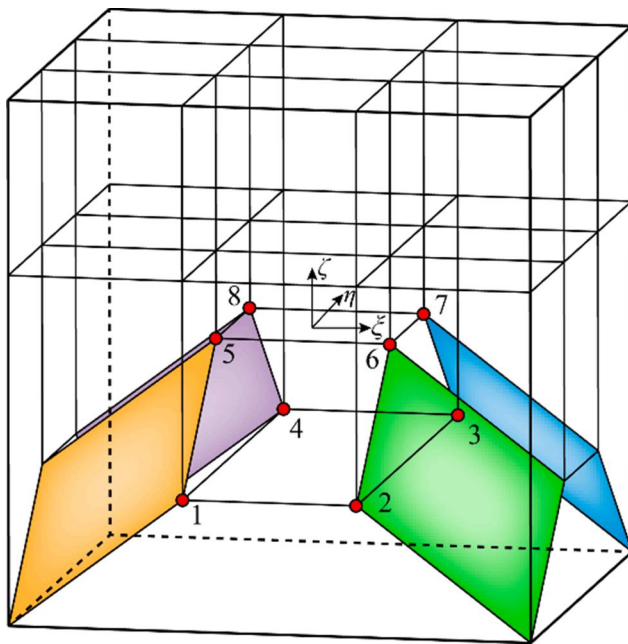


Fig. 7. Subdivision details of refinement template (c) shown in Fig. 6. The red dots represent parts of the inserted nodes at specified locations. Four faces are plotted in color. Inserted node 2 and node 6 form an edge of the green face. Node 3 and node 7 form an edge of the blue face. Node 4 and node 8 form an edge of the purple face. Node 5 and node 1 form an edge of the orange face.

coordinate system along the cubic spline  $f$ ; both the error measure weights  $\hat{w}_i$  and the piecewise constant weight function  $\lambda$  equal 1;  $p$  is the smoothing factor taken as 0.95 in this paper; and  $D^2f$  represents the second derivative of function  $f$ . After obtaining the spline  $f$ , the smoothed front vertices  $v'_i$  ( $i = 2, \dots, n - 1$ ) can be directly obtained [66]. Attention should be paid to  $v'_1$  and  $v'_n$  because two adjacent crack front segments share the same segmentation point. In this

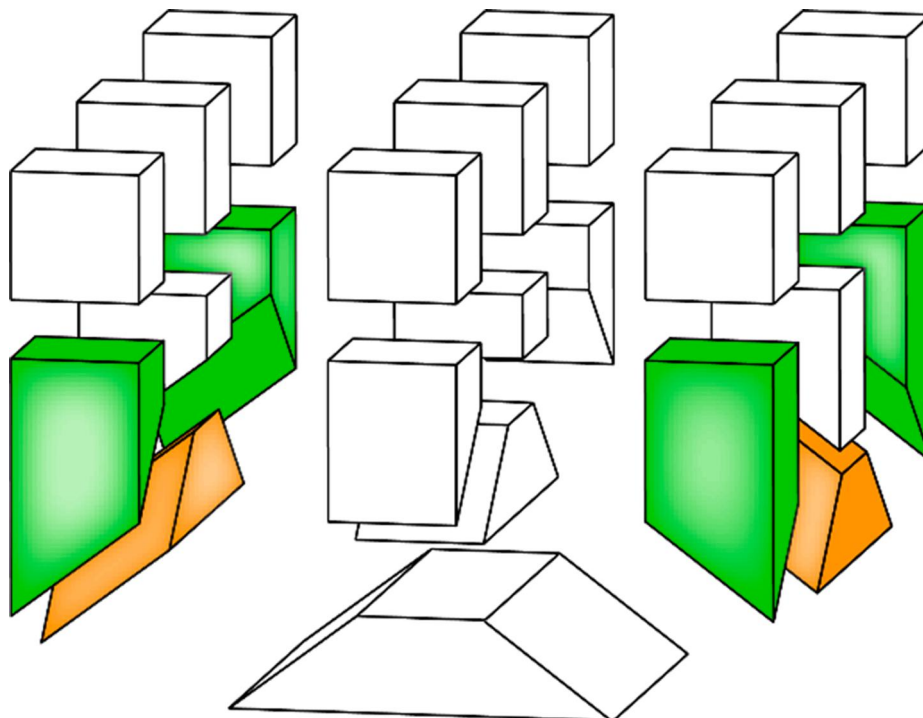


Fig. 8. Illustration of the 22 subdivided elements of refinement template (c) shown in Fig. 6.

study,  $v'_1$  is obtained by taking the average value of the first smoothed vertex belonging to the cubic spline (the red solid spline) and the last smoothed vertex belonging to its neighboring cubic spline (the left red dotted spline).

### 3.3. Numerical integration and element partitioning

The standard Gauss integration with more Gauss points [67] can be used to perform numerical integration of enriched elements. However, since the noncontinuity of enrichment functions, the standard Gauss integration may lead to inaccurate results. Furthermore, if one subsection of the element divided by the crack surface contains no integration point, which is quite likely to happen, the integration accuracy can be substantially undermined. Therefore, in this study, the enriched elements are partitioned into a set of tetrahedrons [67] across the crack surface to perform numerical integration with 4 integration points [30] in order to enhance the accuracy and convergence rate of the proposed numerical model. For standard elements and blending elements,  $2 \times 2 \times 2$  and  $6 \times 6 \times 6$  Gauss points [30] are utilized to perform the numerical integration, respectively.

In this section, we focus on the partitioning procedure of enriched

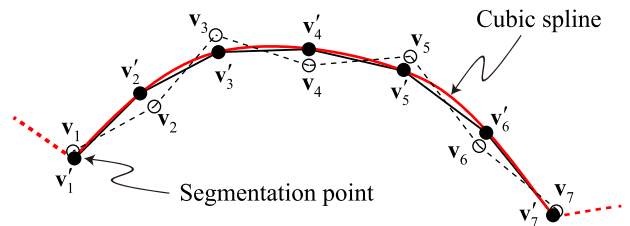


Fig. 9. Illustration of the smoothness of vertices (from  $v_1$  to  $v_7$ ) of a crack front segment. The black dotted line and the black solid line represent the initial crack front and the smoothed crack front, respectively. The red solid line represents the smoothing cubic spline of the segment. The left and right red dotted lines denote the smoothing cubic spline of the adjacent segments.

elements containing segmentation points in the framework of explicit description of crack surface. For other scenarios, readers are referred to our recent paper [30]. As shown in Fig. 10a, the explicit crack included in the tip-enriched element is composed of 6 triangular patches, i.e.,  $P_s-P_1-P_2$ ,  $P_s-P_2-I_1$ ,  $P_s-I_1-P_3$ ,  $P_s-P_3-P_4$ ,  $P_3-I_2-P_4$ , and  $P_s-P_4-P_5$ , where  $P_s$  is the segmentation point,  $I_1$  and  $I_2$  are intersections of element edges and crack surface, and  $P_1$  to  $P_5$  are intersections of element faces and crack surface. As illustrated in Fig. 10b to 10e, a typical partitioning procedure of a tip-enriched element that contains a segmentation point follows:

- (1) Let point  $P_e$  be the intersection of the angular bisector of angle  $P_1-P_s-P_5$  and element face, then generate triangular patches  $P_s-P_e-P_1$  and  $P_s-P_5-P_e$ , as shown in Fig. 10b.
- (2) Generate triangular patches  $I_3-P_1-P_e$  and  $I_4-P_e-P_5$  by extending  $P_s-P_e-P_1$  and  $P_s-P_5-P_e$ , respectively, as shown in Fig. 10c, where  $I_3$  and  $I_4$  are intersections of element edge and planes of triangles  $P_s-P_e-P_1$  and  $P_s-P_5-P_e$ , respectively.
- (3) Subdivide the enriched element into the upper sub-element (Fig. 10d) and the lower sub-element (Fig. 10e).
- (4) Perform polygon triangulation for the surfaces of the upper and lower sub-elements, as shown by the red lines in Fig. 10d and 10e.
- (5) Create a point at the centroid (taken as the arithmetic mean of the coordinates of all points that make up the sub-element) of each sub-element.
- (6) For each sub-element, construct tetrahedrons by connecting points of triangles and the newly created points.

### 3.4. Program flow

The proposed numerical strategy follows the following steps:

- (1) Determine enriched elements according to the geometrical configuration of the crack surface [30].
- (2) Perform local mesh refinement (Section 3.1) for enriched elements with tip-enriched nodes.
- (3) Partition the enriched elements to perform numerical integration (Section 3.3).
- (4) Solve the linear system to get the displacement field.

- (5) Calculate the stress tensors of all Gauss integration points.
- (6) Update crack front vertexes according to the maximum principal stress criterion (Section 2.2).
- (7) Perform cubic spline curve fitting of crack front vertexes (Section 3.2).
- (8) Go to step (1) until all propagation steps have been simulated.

## 4. Verification and numerical examples

The proposed numerical strategy is implemented in an in-house program named PhiPsi (<http://phipsi.top/>) which is written in Fortran. The linear system is solved using the preconditioned conjugate gradient (PCG) method in an element-by-element manner [68]; thus, the memory-consuming assembly of the global stiffness matrix can be avoided. Besides, shared-memory parallel computing, i.e., OpenMP, is adopted to accelerate the computation. In this section, after verification of the proposed strategy, several examples will be presented to show the pervading and non-negligible effects of crack front segmentation.

### 4.1. Verification of local mesh refinement scheme

We consider the propagation of an edge crack in a plate subjected to a tensile load  $\sigma = 1$  MPa to verify the local mesh refinement scheme described in Section 3.1. As shown in Fig. 11, the width ( $W$ ), height ( $H$ ), and thickness ( $T$ ) of the plate are taken as 0.5 m, 1 m, and 0.1 m, respectively. The length ( $a$ ) of the initial crack is set to 0.1 m. The elasticity modulus  $E$  and Poisson's ratio  $\nu$  are 50 GPa and 0.3, respectively. The crack propagates for 4 steps over a length of 0.05 m for each step. The mode-I SIF ( $K_I$ ) along the crack front is computed using the displacement extrapolation method [30] and then compared with the following analytical solution [69]:

$$K_I = f(a/W)\sigma\sqrt{a} \tag{17}$$

where

$$f(a/W) = 1.99 - 0.41\left(\frac{a}{W}\right) + 18.7\left(\frac{a}{W}\right)^2 - 38.48\left(\frac{a}{W}\right)^3 + 53.85\left(\frac{a}{W}\right)^4 \tag{18}$$

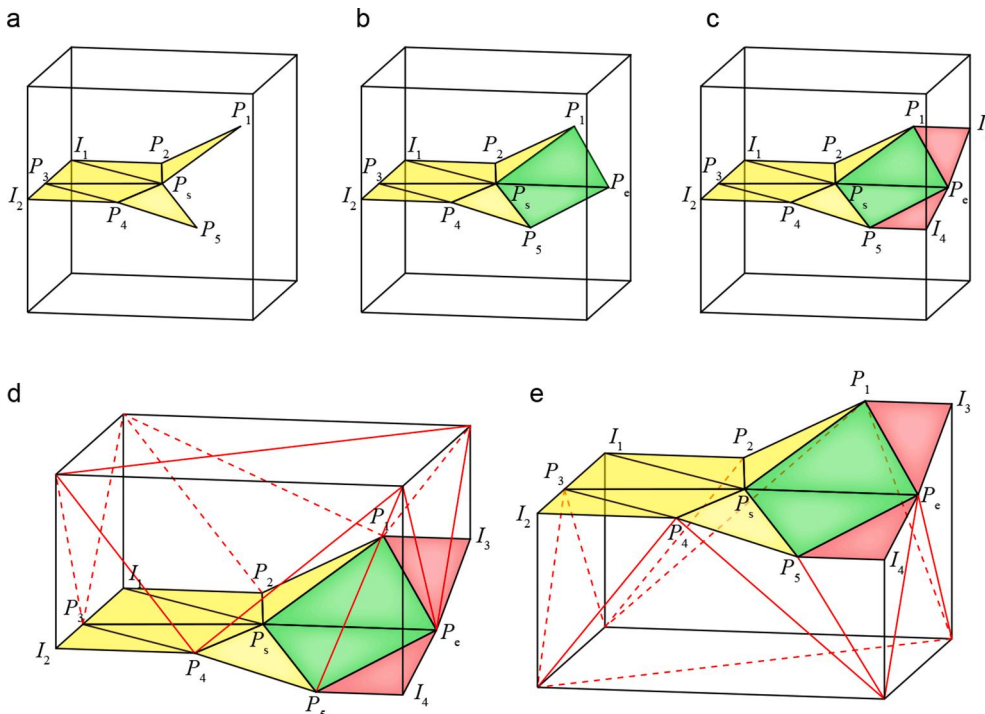


**Fig. 10.** Illustration of partitioning procedure of an enriched element containing a segmentation point  $P_s$ . (a) The tip-enriched element and the explicit crack included in the element. (b) Generation of triangular patches (colored in green)  $P_s-P_e-P_1$  and  $P_s-P_5-P_e$ , where  $P_e$  is the intersection of the angular bisector of  $P_1-P_s-P_5$  and element face. (c) Generation of triangular patches (colored in red)  $I_3-P_1-P_e$  and  $I_4-P_e-P_5$  by extending triangular patches  $P_s-P_e-P_1$  and  $P_s-P_5-P_e$ , respectively. (d) The upper sub-element. (e) The lower sub-element.

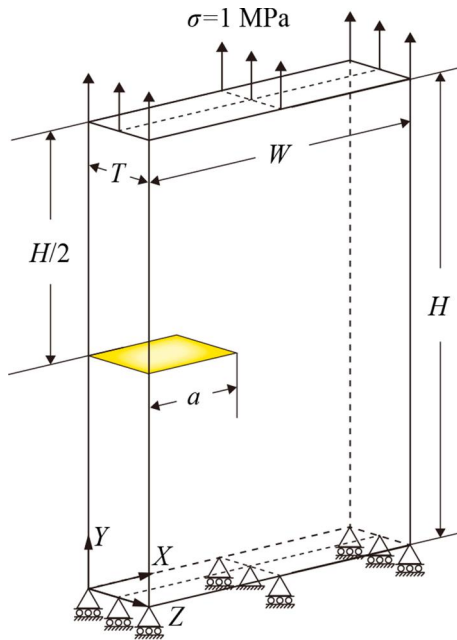


Fig. 11. The geometry and boundary conditions of a plate with a rectangle edge crack.

Four different mesh configurations (i.e., (a)  $7 \times 17 \times 4$  in  $W, H$ , and  $T$  directions, respectively, similarly hereinafter; (b)  $9 \times 23 \times 4$ ; (c)  $13 \times 33 \times 4$ ; and (d)  $19 \times 47 \times 4$ ) are selected to perform the simulation. The average SIFs at vertexes along the front of the initial crack and the final crack after 4 propagation steps are shown in Figs. 12 and 13, respectively. In both figures, in addition to the analytical solution (denoted by Analytical), results obtained using the XFEM without local refinement (denoted by XFEM), the XFEM with geometrical enrichment for an enrichment radius of 0.1 m [30] (denoted by XFEM with geometrical enrichment), and the XFEM with local refinement (denoted by XFEM with local refinement) are presented. It can be found that the XFEM with local refinement gives the best performance towards the analytical solution. It can also be noticed that the proposed local refinement scheme shows higher accuracy than the widely used geometrical enrichment scheme [30,70]. Meshes after local refinement for the final crack of the initial mesh configuration (c) are shown in Fig. 14, from which we can notice that mesh conformities are all satisfied. Variation of average  $K_I$

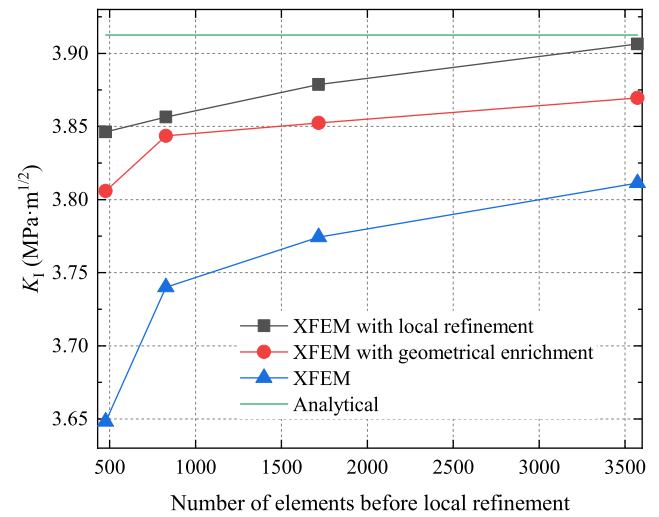


Fig. 13. Variation of average  $K_I$  along the front of the final crack with the number of elements (before local refinement) of initial mesh configurations.

along the crack front versus crack length obtained from mesh configuration (d) is shown in Fig. 15, in which analytical solution as well as the relative errors are also presented. Good agreements and low relative errors can be observed, indicating the applicability and accuracy of the proposed local mesh refinement scheme.

Fig. 16 presents the X-Z view of contours of the final crack aperture obtained from mesh configuration (d). The maximum aperture of Fig. 16a and b are 0.1905 mm and 0.1930 mm, respectively. In addition, the maximum aperture obtained using FRANC3D [71] with a fine-enough mesh is 0.1928 mm. The relative error compared to the FRANC3D solution reduces from 1.24% when using the XFEM to 0.104% when using the XFEM with local refinement. It can also be seen from Fig. 16 that the XFEM with local refinement achieves a better resolution of displacement field around the crack front, which is of great importance for the crack front segmentation simulation.

#### 4.2. Verification of crack propagation criterion

In this section, a benchmark problem [31,72] shown in Fig. 17 is simulated to verify the proposed crack propagation criterion and determine the befitting value of parameter  $\chi$  in the weight function (Eq. (13)). The Y and Z coordinates of the initial crack front are taken as 24.75 mm and 14.42 mm, respectively. Material parameters including  $E$ ,  $\nu$ , and tensile strength  $s_t$  are taken as 25 GPa, 0.18, and 2.5 MPa [72], respectively. As shown in Fig. 18, the model is discretized into 3,675 hexahedral elements before performing local mesh refinement. The length of propagation step ( $\Delta a_{max}$ ) is taken as 15 mm and the simulation stops after 15 propagation steps.

Comparison of crack propagation paths predicted using different  $\chi$  (i.e., 0.5, 1.5, 5, and 50) for the cases with and without local mesh refinement is presented in Fig. 19, where the upper and lower ranges of experimental results [72] are also shown. In addition to the path when  $\chi$  equals 50 without local mesh refinement, obviously, all predicted paths are within the range of experimental results, revealing the flexibility and robustness of the proposed crack propagation criterion. The computed paths in the cases without local mesh refinement seem to be quite zigzag in shape, especially when  $\chi$  equals 0.5 and 50, which is not surprising since the mesh is relatively coarse, as shown in Fig. 18. In the meantime, the proposed local mesh refinement algorithm can significantly smooth the propagation paths. It can be found that  $\chi = 5$  gives the smoothest path (see the red solid line in Fig. 19) which at the same time fits well with the median line of the experimental range. Furthermore, the best consistency between paths with and without local mesh refinement occurs when  $\chi = 5$ . Thus,  $\chi$  is taken as 5 in all of the following examples

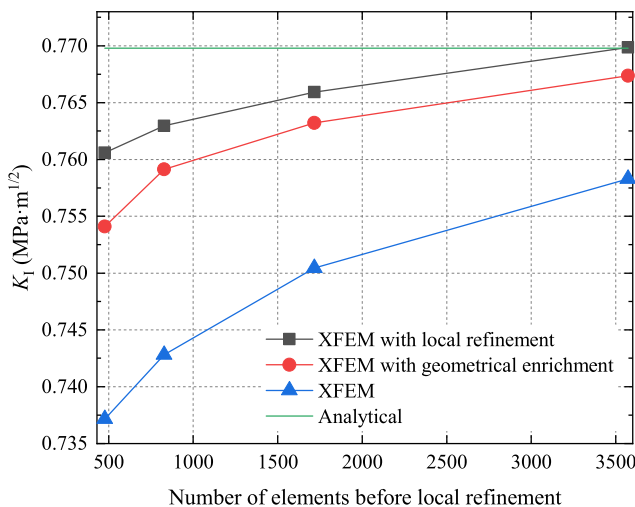
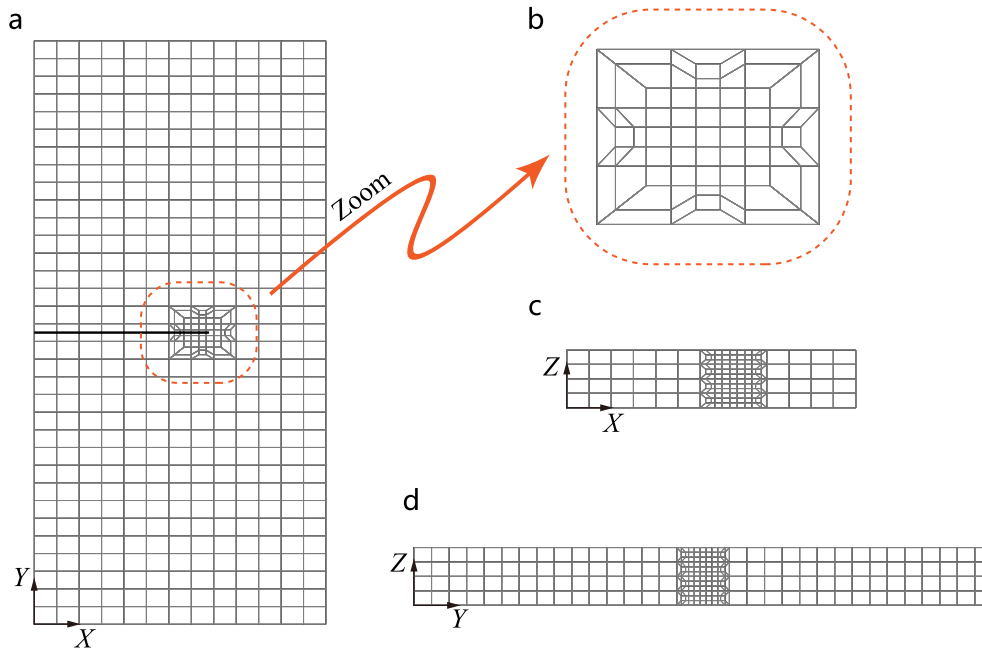
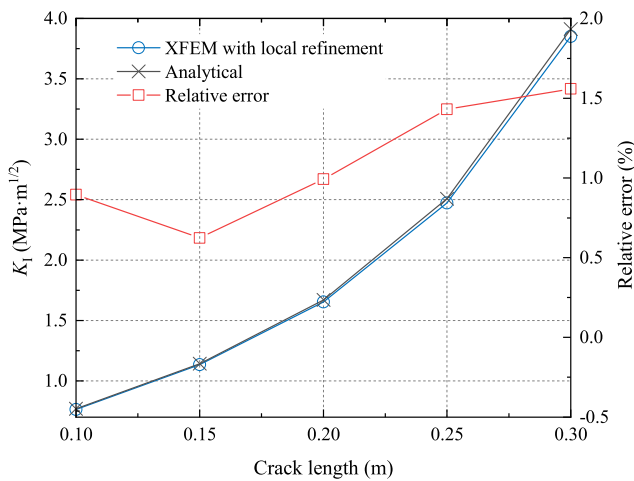


Fig. 12. Variation of average  $K_I$  along the front of the initial crack with the number of elements (before local refinement) of initial mesh configurations.



**Fig. 14.** Mesh after local refinement for the final crack of initial mesh configuration (c). (a) X-Y view where the black line represents the crack surface; (b) Zoom view of refined mesh in the X-Y view; (c) X-Z view; and (d) Y-Z view. The number of elements of the initial mesh is 1,716 and the number of added elements after local refinement is 600.



**Fig. 15.** Average  $K_I$  along the crack front versus crack length. Results obtained from mesh configuration (d). Relative errors between the numerical and analytical solutions are also shown.

in this paper. Finally, the contour of crack aperture after 15 propagation steps when  $\chi$  equals 5 is given in Fig. 20, where the maximum aperture equals 0.161 mm.

### 4.3. Simulation of three-points bending experiment

Lazarus et al. [1,73] carried out a three-point bending fatigue experiment to investigate the propagation of an initial skew crack in a beam made of a typical brittle material (PMMA). As shown in Fig. 21, the height of the initial crack is 20 mm. The intersection angle between the crack surface and the mid-plane ( $Y = 0$ , see Fig. 21 for the coordinate system) of the beam is 45°. A force  $F$  is monotonically applied in the middle of the top surface. Material parameters including  $E$ ,  $\nu$ ,  $s_b$ , and  $K_{Ic}$  are taken as 2.8 GPa, 0.3, 15 MPa, and 1.24 MPa·m<sup>1/2</sup>, respectively [1,31]. A mesh with 9,108 hexahedral elements is adopted to perform

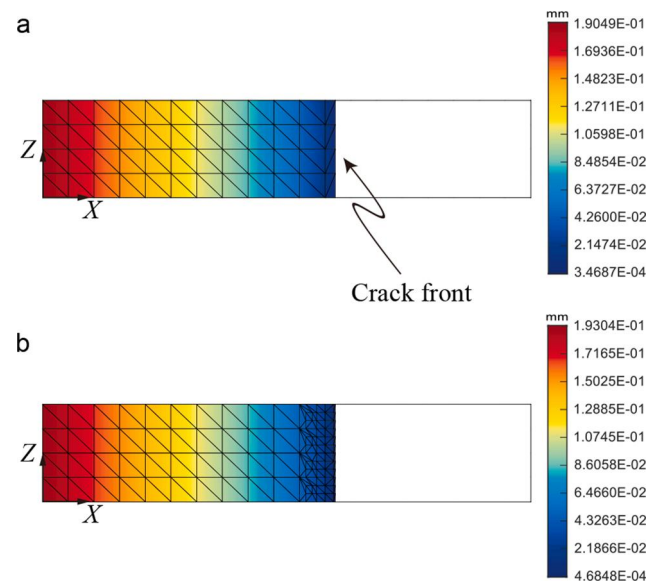


**Fig. 16.** X-Z view of contours of the final crack aperture obtained from mesh configuration (d). (a) XFEM; and (b) XFEM with local refinement. The discretization meshes [30] of the crack surface to calculate the crack aperture are also shown.

the simulation which stops after 20 propagation steps. The crack propagation length is taken as 1.2 mm. The SIFs along the crack front are calculated using the displacement extrapolation method [30]. The local mesh refinement algorithm, as well as the cubic spline curve fitting technique, are adopted in this example. It should be noted that the principal aim of this example is not to reproduce the segmentation process, but to assess the ability of the proposed strategy to deal with mixed-mode fracture.

The computed crack propagation paths are presented in Fig. 22, in which the experimental results are also shown. It can be observed that the cracks twist sharply and then propagate in a pure mode-I state, and

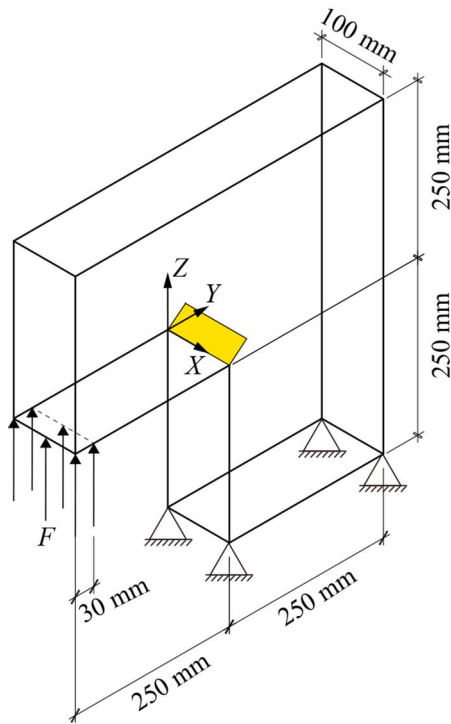


Fig. 17. Geometry and boundary conditions of an L-shaped panel. The yellow surface represents the initial crack.

two propagation paths coincide well with each other. To make a quantitative comparison, positions of crack front in the  $Y = 5 \text{ mm}$  plane are given in Fig. 23. It can be seen that the path obtained using the maximum principal stress criterion agrees well with the experimental one [73]. From the above comparisons, it can be confirmed that the proposed numerical strategy with parameter  $\chi$  equals 5 is capable of predicting 3D crack propagation paths in mixed mode.

#### 4.4. Comparison of crack paths with and without considering segmentation

In this section, simulations of crack propagation under mixed I-II-III loading conditions will be performed to study the effects of segmentation on the geometrical evolution process of the crack surface. As shown in Fig. 24, the size of the model is  $50 \times 50 \times 50 \text{ m}$ . Tensile stress  $\sigma = 5 \text{ MPa}$  is applied on the top surface. The radius ( $a$ ) of the initial inclined penny-shaped crack is  $2.5 \text{ m}$ . The incline angle  $\alpha$  is  $45^\circ$ . The position angle  $\gamma$  in Fig. 24c is used to differentiate the location of the crack front. The elasticity modulus  $E$ , Poisson's ratio  $\nu$ , and tensile strength  $s_t$ , are taken as  $20 \text{ GPa}$ ,  $0.2$ , and  $5 \text{ MPa}$  respectively. The model is meshed with  $25,725$  hexahedral elements. The crack propagation length is taken as  $0.25 \text{ m}$ . The simulation continues after 8 propagation steps.

As shown in Fig. 25, the SIFs along the front of the initial crack can be obtained according to the following analytical expressions [74]:

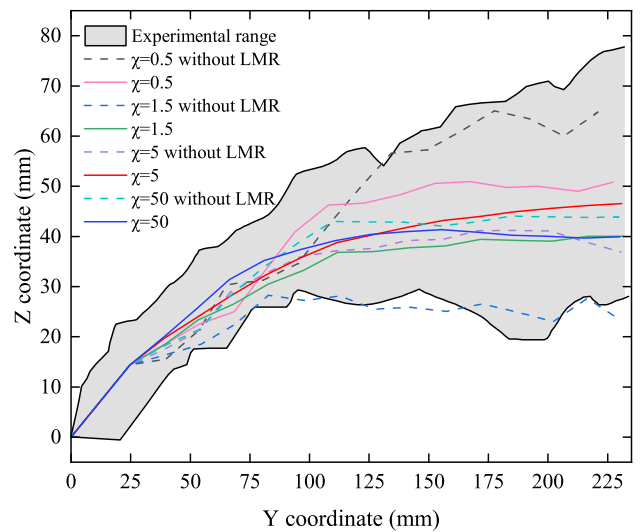


Fig. 19. Comparison of crack propagation paths in the  $X = 0$  plane. LMR is short for local mesh refinement.

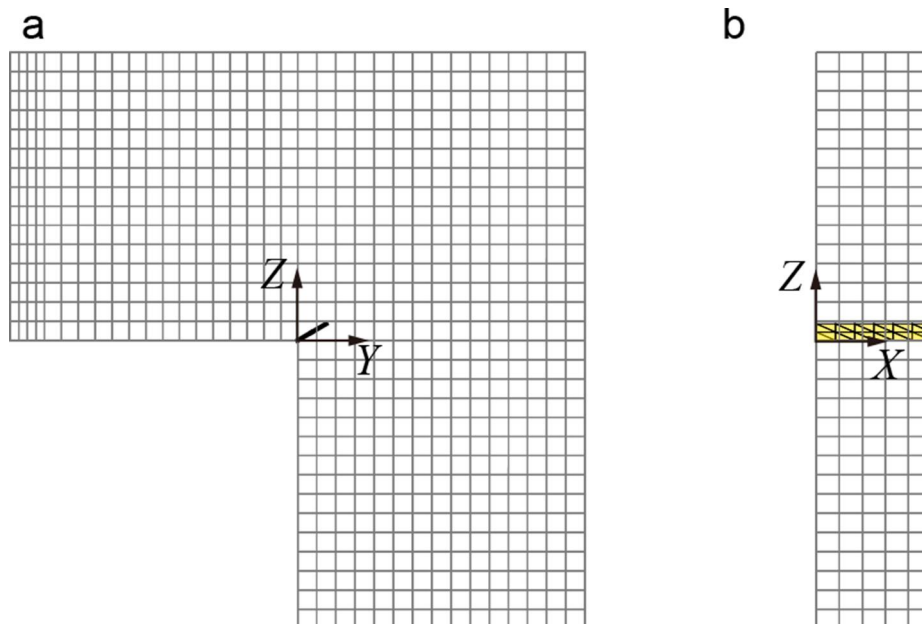


Fig. 18. Finite element mesh of the L-shaped panel. (a) Y-Z view and (b) X-Z view. The bold black line in figure (a) represents the initial crack surface.

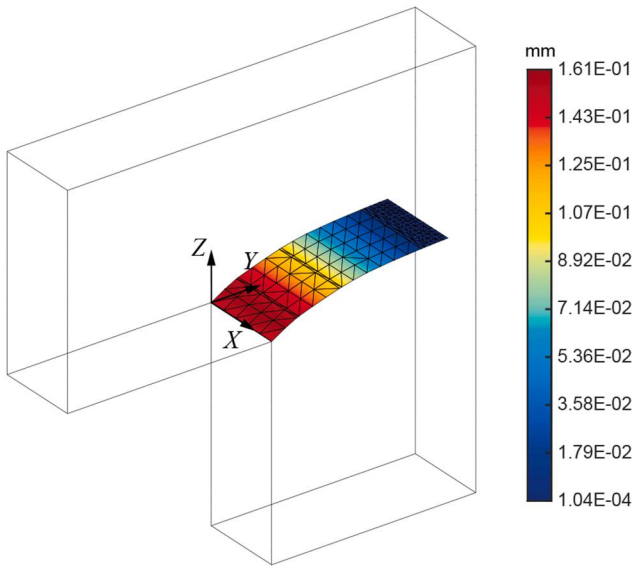


Fig. 20. Contour of crack aperture after 15 propagation steps.  $\chi$  is taken as 5.

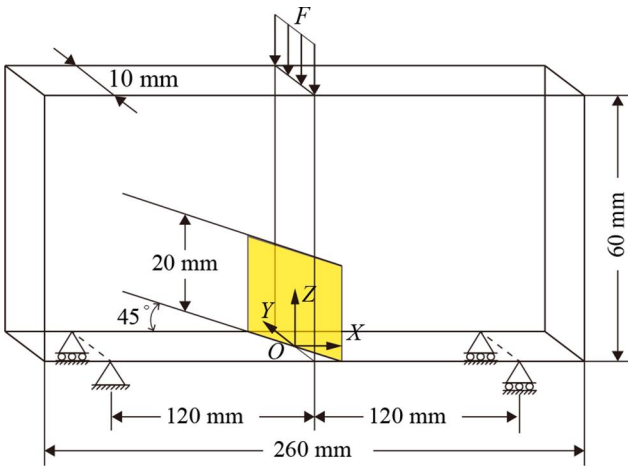


Fig. 21. Geometry and boundary conditions of a three-point bending beam with an initial skew crack.

$$\begin{cases} K_I = 2\sigma\cos^2\alpha\sqrt{\frac{a}{\pi}} \\ K_{II} = -\frac{4}{2-\nu}\sigma\sin\alpha\cos\alpha\sqrt{\frac{a}{\pi}}\sin\gamma \\ K_{III} = -\frac{4(1-\nu)}{2-\nu}\sigma\sin\alpha\cos\alpha\sqrt{\frac{a}{\pi}}\cos\gamma \end{cases} \quad (19)$$

It can be seen from Fig. 25 that under the action of stress  $\sigma$ , crack front tips with  $\gamma = 0$  and  $\pi$  are in mode I-II, while crack front tips with  $\gamma = \pi/2$  and  $3\pi/2$  are in mode I-III, hence segmentation might be triggered. It should be noted that determination of the number of segments (or the segment length) is a challenging task since it is closely related to the shape and scale of the initial crack, the loading conditions, the material type [36], and even initial defects [6]. Therefore, in this study, four segmentation points ( $\gamma = 2\pi/5, 3\pi/5, 7\pi/5$  and  $8\pi/5$ ) are directly specified. Notably different propagation paths with and without considering crack front segmentation are presented in Fig. 26. It can be seen in Fig. 26b that segments in the mode I-III zone rotate towards the direction of the applied tensile stress, resulting in more complex crack morphology compared to the one shown in Fig. 26a. It can also be noticed that crack surfaces in the mode I-II zone are similar in both

figures.

#### 4.5. Hydraulic fracturing simulation

Hydraulic fracturing treatment is widely used in oil and gas industries to improve the permeability of reservoirs and thus to enhance well productivity. In the literature, the hydraulic fracture in 3D simulations is generally treated as a single crack without branching or segmentation. Nevertheless, as shown in Fig. 1c, the crack front segmentation phenomenon has been extensively observed by researchers in the laboratory for a long time [14–16]. In this section, we perform hydraulic fracturing simulations in laboratory-scale and study the effects of crack front segmentation process.

As shown in Fig. 27, the radius ( $R$ ) of a transparent cylindrical specimen made of PMMA is 5 cm. The height of the specimen is 20 cm. A borehole is drilled along the axis of the cylinder and cased with a metal pipe. An initial circular fracture with a radius ( $a$ ) of 1.25 cm is perpendicularly positioned to the borehole. The top surface of the specimen is fixed and a torque ( $T$ ) of 500 N·m is applied on the bottom surface to generate mode-III loading condition. Therefore, after pumping the fluid, the mixed-mode I-III loading conditions can be reached. Since the axial symmetry of the specimen, the ratio of  $K_{III}/K_I$  is constant along the crack front before segmentation occurs. The elasticity modulus  $E$ , Poisson's ratio  $\nu$ , tensile strength  $s_b$  and fracture toughness  $K_{Ic}$  of PMMA are taken as 3.32 GPa, 0.38, 40 MPa, and 1.21 MPa·m<sup>1/2</sup>, respectively [22,75]. The liquid injection rate ( $Q$ ) is 0.006 mL/min. The viscosity of the injected liquid is 0.01 Pa·s and the injection continues until the time reaches 70 min. Wu [22] performed experiments similar to the one described here, but a quantitative comparison is not available for the lack of some essential experimental information. However, the phenomenon and conclusions reported in Wu's experiments [22] will be used as a reference.

Submitting the fracturing parameters into analytical solutions [76] of circular fluid-driven fractures, it can be supposed that the fluid pressure is uniform [22] inside the fracture. Hence, without considering segmented crack front, according to the analytical solution of a uniformly pressurized circular crack inside a round bar [77], the evolution of crack radius  $r_c$  and fluid pressure  $P$  over injection time  $t$  can be obtained after some manipulations:

$$r_c(t) = \begin{cases} a, & \text{if } t \leq t_s \\ \left( \frac{3QE t}{8\sqrt{\pi}(1-\nu^2)K_{Ic}} \right)^{2/5}, & \text{if } t > t_s \end{cases} \quad (20)$$

$$P(t) = \begin{cases} \frac{3QE t}{16a^3(1-\nu^2)G\left(\frac{a}{R}\right)}, & \text{if } t \leq t_s \\ \frac{\sqrt{\pi}K_{Ic}}{2\sqrt{r_c}F\left(\frac{r_c}{R}\right)}, & \text{if } t > t_s \end{cases} \quad (21)$$

where  $t_s$  represents the injection time when the initial fracture starts to propagate and can be calculated by

$$t_s = \frac{8\sqrt{\pi}(1-\nu^2)K_{Ic}a^{5/2}}{3EQ} \quad (22)$$

Functions  $G$  and  $F$  take the following forms, respectively:

$$G\left(\frac{a}{R}\right) = \frac{1}{(a/R)^3} \left[ 1.26 \ln\left(\frac{1}{1-a/R}\right) - 1.26\frac{a}{R} - 0.63\left(\frac{a}{R}\right)^2 + 5.8\left(\frac{a}{R}\right)^3 - 0.315\left(\frac{a}{R}\right)^4 - 0.102\left(\frac{a}{R}\right)^5 + 0.063\left(\frac{a}{R}\right)^6 \right] \quad (23)$$

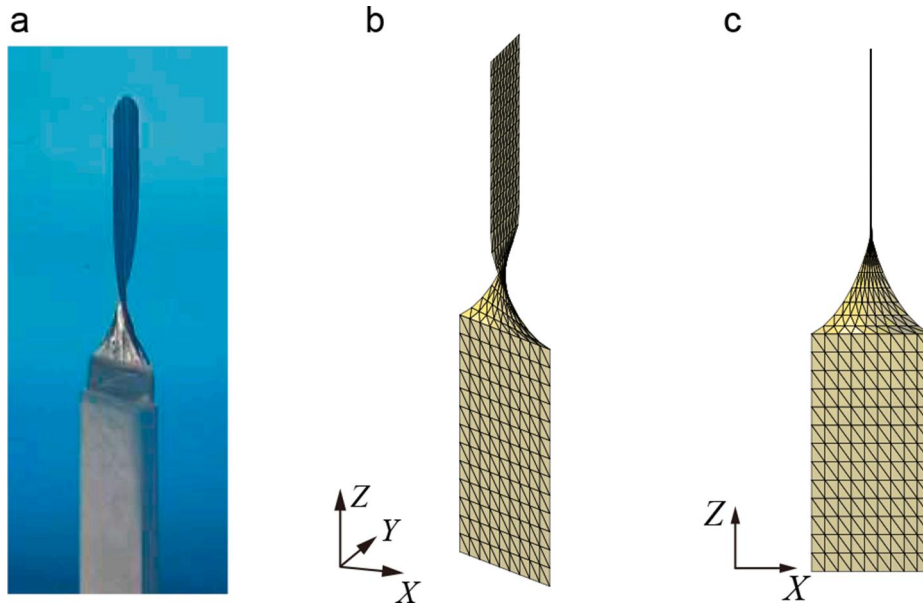


Fig. 22. Crack propagation paths obtained from (a) the experiment [1], (b) the numerical results, and (c) the X-Z view of the numerical results.

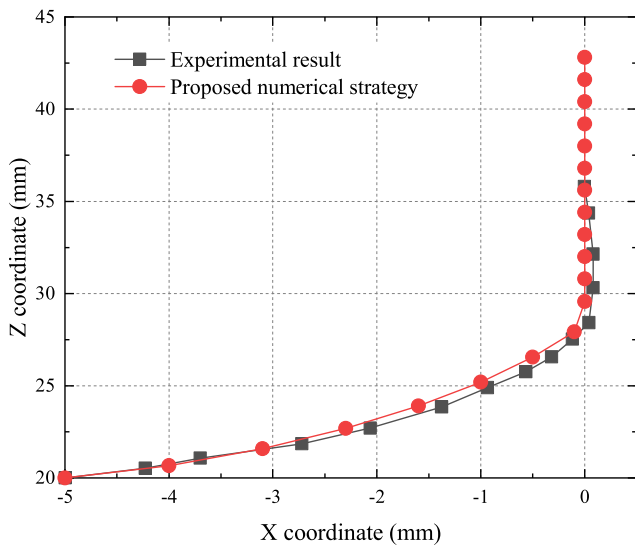


Fig. 23. Positions of crack front in the  $Y = 5$  mm plane.

$$F\left(\frac{r_c}{R}\right) = \frac{1 - \frac{r_c}{2R} + 0.148\left(\frac{r_c}{R}\right)^3}{\sqrt{1 - \frac{r_c}{R}}} \quad (24)$$

The SIFs  $K_I$  and  $K_{III}$  of the initial crack can be estimated according to the following equations [77]:

$$K_I = \frac{2}{\pi} P(t) \sqrt{\pi a}, \quad K_{III} = \frac{4}{3\pi} \tau \sqrt{\pi a} \quad (25)$$

where  $\tau$  is the shear stress caused by the torque  $T$  and can be calculated by

$$\tau = \frac{2Ta}{\pi R^4} \quad (26)$$

Thus, the ratio of  $K_{III}/K_I$  can be estimated using

$$\frac{K_{III}}{K_I} = \frac{4Ta}{3\pi P(t)R^4} \quad (27)$$

The model is regularly meshed into 27,040 hexahedral elements. The

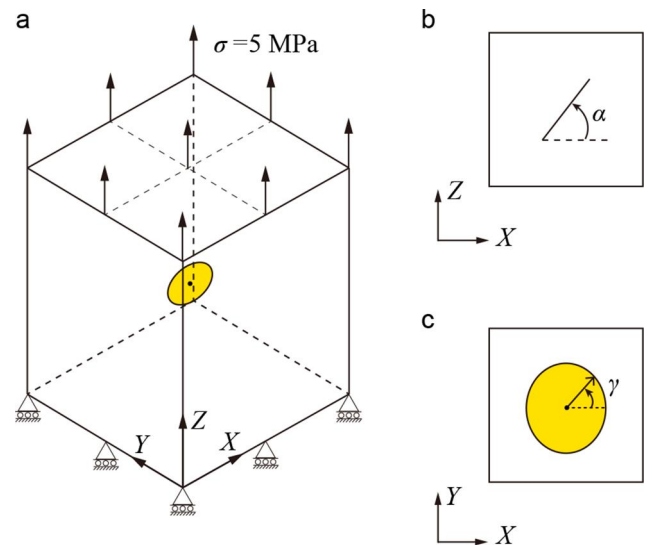


Fig. 24. Illustration of an inclined penny-shaped crack inside a cubic model. (a) The applied force and boundary conditions; (b) the X-Z view of the zoomed crack; and (c) the X-Y view of the zoomed crack.

crack propagation length is set to 0.2 cm. For each propagation step, the constant fluid pressure inside the crack is determined using the bisection method [78] until the crack propagation criterion is satisfied [79]. In order to study the effects of crack front segmentation on hydraulic fracturing, simulation cases without considering segmentation (case 1), with 5 crack front segments (case 2), and with 7 crack front segments (case 3) are comparatively performed. In case 1, the torque is not applied to provide a pure mode-I loading condition which is consistent with the above presented analytical solutions. In cases 2 and 3, however, all segments are evenly spaced along the crack front. According to Eq. (21), the injection pressure required to trigger the crack propagation is 9.45 MPa. Then, using Eq. (27), the ratio of  $K_{III}/K_I$  can be calculated as 4.49%. The injection pressure curves over time are shown in Fig. 28. A fairly close agreement between the results of case 1 and the analytical solution can be observed. Besides, it can be clearly seen that the injection pressure dramatically increases as the number of crack front

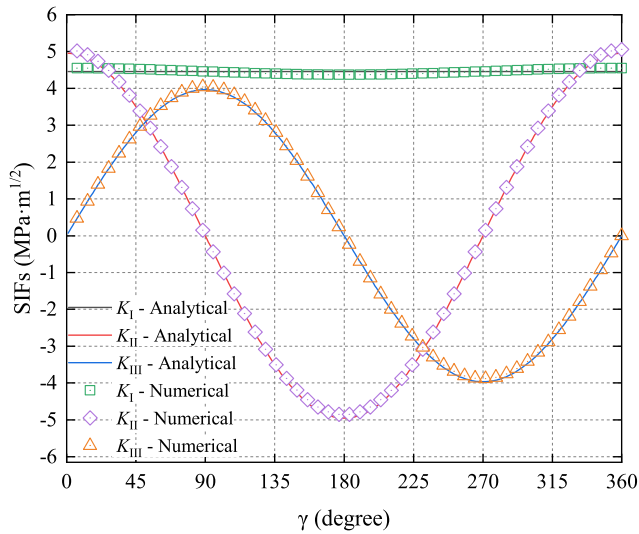


Fig. 25. Variations of SIFs along the front of the initial crack. Both the analytical results and the numerical results are presented.

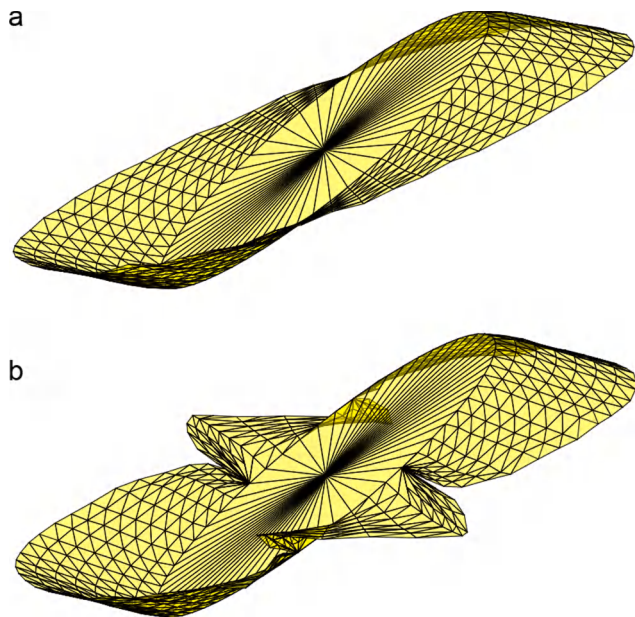


Fig. 26. Comparison of the final propagation paths without (a) and with (b) considering crack front segmentation.

segments increases from 0 to 5, and then to 7. Specifically, the final injection pressure increases by 76.5% from 3.71 MPa in case 1 to 6.55 MPa in case 2, and then further increases by 15.4% to 7.56 MPa in case 3 compared to case 2. The phenomenon of pressure increase observed here in numerical simulation is in accordance with the experimental results reported by Wu [22].

One of the segmented fractures obtained in the experiment [22] is shown in Fig. 29, in which 7 daughter cracks can be observed. In the meantime, the final simulated fracture surface with 7 segments is presented in Fig. 30. From both figures, it can be seen that segments are inclined at a small angle with respect to the initial fracture. In addition, overlapping between adjacent segments can be noticed. It is well known that stress shadow effects exist between two neighboring fractures during hydraulic fracturing and significantly affect the behavior of fracture growth [80]. Therefore, it can be conjectured that the interactions between overlapped segments and the resulting stress shadow

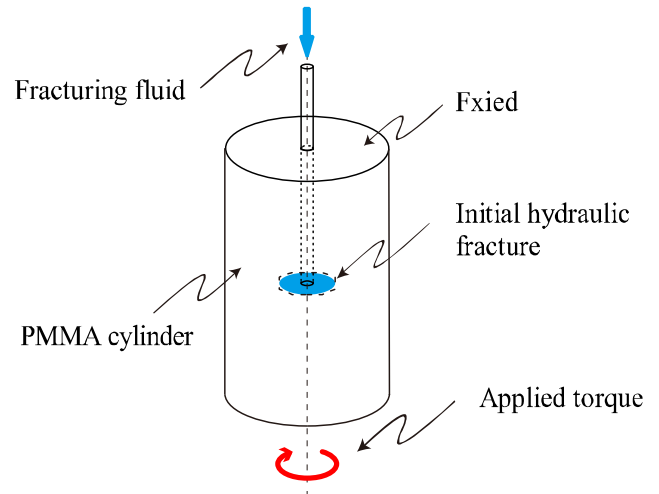


Fig. 27. Illustration of the hydraulic fracturing experiment of a cylindrical PMMA specimen under mixed-mode I-III loading [22].

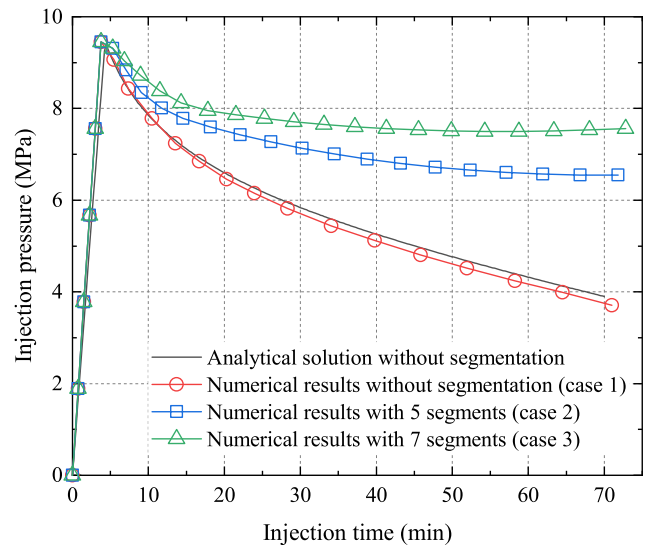


Fig. 28. Comparisons of injection pressure curves over time.

effects might be one of the primary causes for the increase of fluid pressure as shown in cases 2 and 3 in Fig. 28. Besides, the unbroken section between segments will prevent the fracture from opening, thus restricting the fluid flow, and higher pressure is required to further propagate the fracture. Accordingly, it can be concluded that ignoring fracture front segmentation for a mixed-mode I-III fluid driven fracture will underestimate the injection pressure, thus leading to unrealistic simulation results.

### 5. Conclusions

The crack front segmentation phenomenon has been widely observed in both laboratory and nature. However, it is difficult to be simulated using the conventional FEM because of the complex geometrical shapes. In this paper, a novel numerical strategy based on the mesh-independent XFEM is proposed, validated, and adopted to simulate the crack front segmentation process. Seeing the features of crack front segmentation, a novel crack propagation criterion based on the weighted average principal stress is utilized to decide the magnitude and direction of crack front advancement. To get a better resolution of the stress field around the crack front, a robust and efficient local mesh refinement scheme

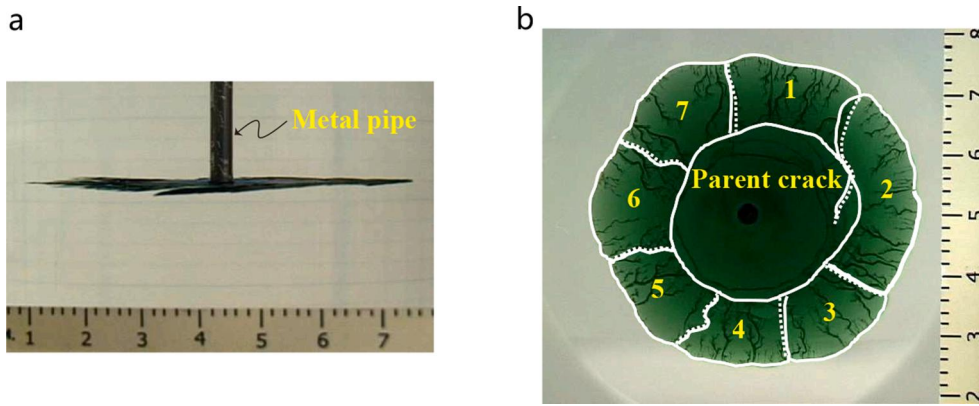


Fig. 29. Fracture with 7 segments obtained in hydraulic fracturing experiment performed by Wu [22]: (a) lateral view and (b) bottom view. Overlapping between segments (for example, segment 1 and segment 2) can be observed in figure (b).

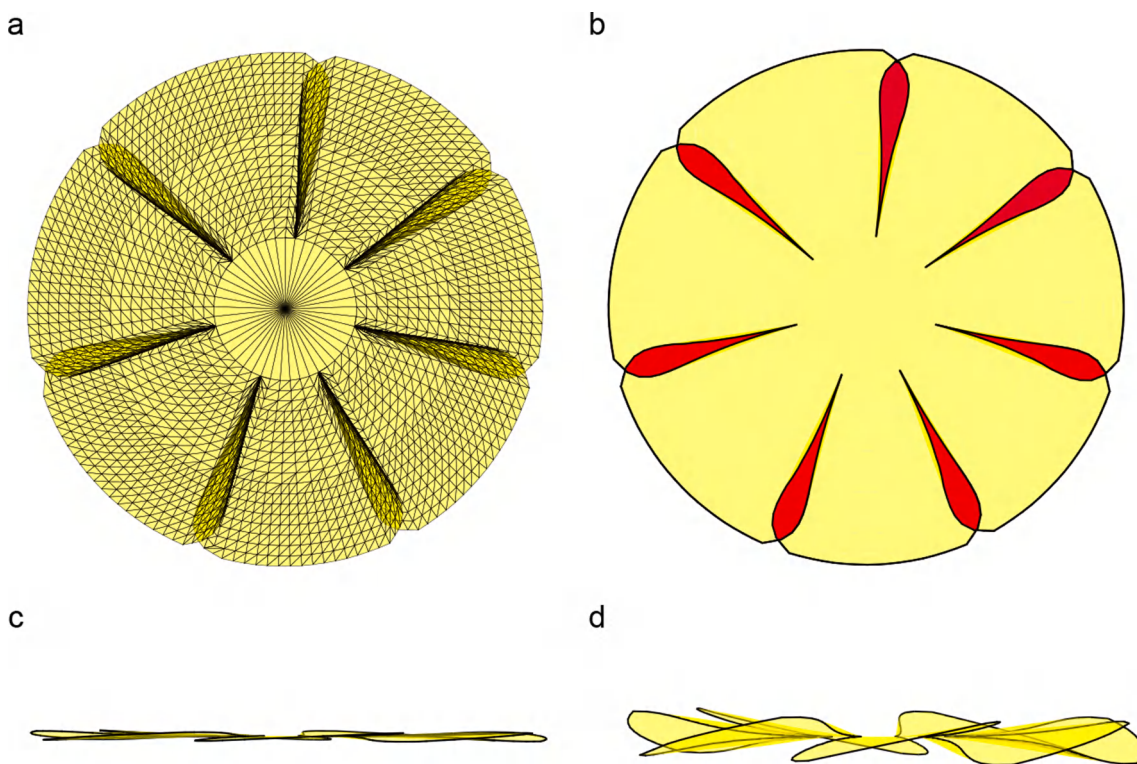


Fig. 30. Fracture with 7 segments obtained in numerical simulation case 3. (a) Bottom view of the crack surface. (b) Bottom view of the crack surface where the portions colored in red highlight the overlapping section between adjacent segments. (c) Lateral view of the crack surface at true deformation scale. (d) Lateral view of the crack surface after 20 times magnification of the deformation.

fully integrated with the XFEM is proposed. Then, a cubic spline curve fitting is performed to smooth the crack front lines within the framework of explicit crack description. The main conclusions are drawn as follows:

- (1) The proposed stress-based propagation criterion in combination with a local mesh refinement scheme is capable of predicting the evolution of crack morphology. Parameter  $\chi$  in the proposed weight function possesses a clear physical meaning and the proposed value ( $\chi = 5$ ) achieves a good matching performance of crack paths with experimental results.
- (2) The local mesh refinement scheme can accurately and robustly capture the stress field evolution around the crack front with better performance compared to the widely adopted geometrical enrichment strategy and can be easily implemented in existing XFEM codes.

- (3) The effectiveness and flexibility of the proposed model are numerically validated by comparing with benchmark problems and experimental results, which indicates that the XFEM is a competent method to simulate the complex phenomenon of crack front segmentation.
- (4) The increase of injection pressure, twisting, and overlapping of crack front segments are observed in the hydraulic fracturing simulation under mode I-III loading conditions. Ignoring fracture front segmentation for a mixed-mode I-III fluid-driven fracture will dramatically underestimate the injection pressure due to the stress shadow effects between adjacent overlapped segments.

### CRedit authorship contribution statement

**Fang Shi:** Conceptualization, Methodology, Software, Validation, Visualization, Investigation, Writing – original draft. **Daobing Wang:** Data curation, Visualization, Writing – review & editing. **Quanquan Yang:** Investigation, Writing – review & editing.

### Declaration of Competing Interest

The authors declare that they have no known competing financial interests or personal relationships that could have appeared to influence the work reported in this paper.

### Acknowledgments

This work was jointly supported by the National Natural Science Foundation of China [Grant No. 51904111]; the Natural Science Foundation of Jiangsu Province [Grant No. BK20170457]; and the Natural Science Research Project of Jiangsu Higher Education Institutions [Grant No. 19KJA150007].

### References

- V. Lazarus, F.G. Buchholz, M. Fulland, J. Wiebesiek, Comparison of predictions by mode II or mode III criteria on crack front twisting in three or four point bending experiments, *Int. J. Fract.* 153 (2008) 141–151.
- T. Cambonie, Y. Klinger, V. Lazarus, Similarities between mode III crack growth patterns and strike-slip faults, *Philos. Trans. Roy. Soc. A* 377 (2018) 20170392.
- A. Eberlein, H.A. Richard, G. Kullmer, Facet formation at the crack front under combined crack opening and anti-plane shear loading, *Eng. Fract. Mech.* 174 (2017) 21–29.
- A. Doitrand, D. Leguillon, Numerical modeling of the nucleation of facets ahead of a primary crack under mode I+III loading, *Int. J. Fract.* 213 (2018) 37–50.
- B. Lin, M.E. Mear, K. Ravi-Chandar, Criterion for initiation of cracks under mixed-mode I + III loading, *Int. J. Fract.* 165 (2010) 175–188.
- K.H. Pham, K. Ravi-Chandar, The formation and growth of echelon cracks in brittle materials, *Int. J. Fract.* 206 (2017) 229–244.
- D.D. Pollard, P.T. Delaney, Formation and interpretation of dilatant echelon cracks, *Geol. Soc. Am. Bull.* 93 (1982) 1291–1303.
- V. Lazarus, B. Prabel, T. Cambonie, J.B. Leblond, Mode I+III multiscale cohesive zone model with facet coarsening and overlap: Solutions and applications to facet orientation and toughening, *J. Mech. Phys. Solids* 141 (2020), 104007.
- C.-H. Chen, T. Cambonie, V. Lazarus, M. Nicoli, A.J. Pons, A. Karma, Crack front segmentation and facet coarsening in mixed-mode fracture, *Phys. Rev. Lett.* 115 (2015), 265503.
- J.-B. Leblond, V. Lazarus, A. Karma, Multiscale cohesive zone model for propagation of segmented crack fronts in mode I+III fracture, *Int. J. Fract.* 191 (2015) 167–189.
- E. Sommer, Formation of fracture ‘lances’ in glass, *Eng. Fract. Mech.* 1 (3) (1969) 539–546.
- W.G. Knauss, An observation of crack propagation in anti-plane shear, *Int. J. Fract. Mech.* 6 (2) (1970) 183–187.
- A.I. Younes, T. Engelder, Fringe cracks: key structures for the interpretation of the progressive Alleghanian deformation of the Appalachian plateau, *GSA Bull.* 111 (1999) 219–239.
- H.H. Abass, S. Hedayati, D.L. Meadows, Nonplanar fracture propagation from a horizontal wellbore: experimental study, *SPE Prod. Oper.* 11 (1996) 133–137.
- M.K. Hubbert, D.G. Willis, Mechanics of hydraulic fracturing, *J. Petrol. Technol.* 9 (1957) 153–168.
- S.D. Hallam, N.C. Last, Geometry of hydraulic fractures from modestly deviated wellbores, *J. Petrol. Technol.* 43 (1991) 742–748.
- M.L. Cooke, D.D. Pollard, Fracture propagation paths under mixed mode loading within rectangular blocks, *J. Geophys. Res.* 101 (1996) 3387–3400.
- O. Ronsin, C. Caroli, T. Baumberger, Crack front echelon instability in mixed mode fracture of a strongly nonlinear elastic solid, *Europhys. Lett.* 105 (2014) 34001.
- J.-B. Leblond, A. Karma, L. Ponson, A. Vasudevan, Configurational stability of a crack propagating in a material with mode-dependent fracture energy - Part I: Mixed-mode I+III, *J. Mech. Phys. Solids* 126 (2019) 187–203.
- K.H. Pham, K. Ravi-Chandar, Further examination of the criterion for crack initiation under mixed-mode I+III loading, *Int. J. Fract.* 189 (2014) 121–138.
- A.J. Pons, A. Karma, Helical crack-front instability in mixed-mode fracture, *Nature* 464 (2010) 85–89.
- R. Wu, L.N. Germanovich, R.S. Hurt, Experimental and theoretical study of mixed-mode I+III crack propagation and segmentation, in: 43rd U.S. Rock Mechanics Symposium & 4th U.S. - Canada Rock Mechanics Symposium, American Rock Mechanics Association, Asheville, North Carolina, 2009.
- T. Cambonie, V. Lazarus, Quantification of the crack fragmentation resulting from mode I+III loading, *Procedia Mater. Sci.* 3 (2014) 1816–1821.
- K.H. Pham, K. Ravi-Chandar, On the growth of cracks under mixed-mode I+III loading, *Int. J. Fract.* 199 (2016) 105–134.
- V. Lazarus, J.-B. Leblond, S.-E. Mouchrif, Crack front rotation and segmentation in mixed mode I + III or I + II + III. Part I: Calculation of stress intensity factors, *J. Mech. Phys. Solids* 49 (7) (2001) 1399–1420.
- V. Lazarus, J.-B. Leblond, S.-E. Mouchrif, Crack front rotation and segmentation in mixed mode I + III or I + II + III. Part II: Comparison with experiments, *J. Mech. Phys. Solids* 49 (7) (2001) 1421–1443.
- J.-B. Leblond, A. Karma, V. Lazarus, Theoretical analysis of crack front instability in mode I+III, *J. Mech. Phys. Solids* 59 (9) (2011) 1872–1887.
- J.-B. Leblond, J. Frelat, Development of fracture facets from a crack loaded in mode I+III: Solution and application of a model 2D problem, *J. Mech. Phys. Solids* 64 (2014) 133–153.
- P. Gupta, C.A. Duarte, Simulation of non-planar three-dimensional hydraulic fracture propagation, *Int. J. Numer. Anal. Methods Geomech.* 38 (2014) 1397–1430.
- F. Shi, J. Liu, A fully coupled hydromechanical XFEM model for the simulation of 3D non-planar fluid-driven fracture propagation, *Comput. Geotech.* 132 (2021), 103971.
- K.P. Wolff, R.L.S. Pitangueira, R.G. Peixoto, A displacement-based and explicit non-planar 3D crack propagation model in the generalized/extended finite element method, *Theor. Appl. Fract. Mech.* 108 (2020), 102647.
- R.N. Thomas, A. Paluszny, R.W. Zimmerman, Growth of three-dimensional fractures, arrays, and networks in brittle rocks under tension and compression, *Comput. Geotech.* 121 (2020), 103447.
- S.B. Biner (Ed.), *Programming Phase-Field Modeling*, Springer International Publishing, Cham, 2017.
- H. Henry, Crack front instabilities under mixed mode loading in three dimensions, *EPL (Europhysics Letters)* 114 (2016) 66001.
- K. Huang, Z. Zhang, A. Ghassemi, Modeling three-dimensional hydraulic fracture propagation using virtual multidimensional internal bonds, *Int. J. Numer. Anal. Methods Geomech.* 37 (2013) 2021–2038.
- C. Meng, F. Maerten, D.D. Pollard, Modeling mixed-mode fracture propagation in isotropic elastic three dimensional solid, *Int. J. Fract.* 179 (2013) 45–57.
- M.L. Hattali, T. Cambonie, V. Lazarus, Toughening induced by the formation of facets in mode I+III brittle fracture: Experiments versus a two-scale Cohesive Zone model, *J. Mech. Phys. Solids* 156 (2021), 104596.
- G. Xu, F. Bower, M. Ortiz, An analysis of non-planar crack growth under mixed mode loading, *Int. J. Solids Struct.* 31 (1994) 2167–2193.
- G. Dhondt, A. Chergui, F.G. Buchholz, Computational fracture analysis of different specimens regarding 3D and mode coupling effects, *Eng. Fract. Mech.* 68 (2001) 383–401.
- F.G. Buchholz, A. Chergui, H.A. Richard, Fracture analyses and experimental results of crack growth under general mixed mode loading conditions, *Eng. Fract. Mech.* 71 (2004) 455–468.
- T. Belytschko, T. Black, Elastic crack growth in finite elements with minimal remeshing, *Int. J. Numer. Methods Eng.* 45 (1999) 601–620.
- N. Moës, J. Dolbow, T. Belytschko, A finite element method for crack growth without remeshing, *Int. J. Numer. Methods Eng.* 46 (1999) 131–150.
- N. Moës, A. Gravouil, T. Belytschko, Non-planar 3D crack growth by the extended finite element and level sets, Part II: Mechanical model, *Int. J. Numer. Methods Eng.* 53 (2002) 2549–2568.
- J.M. Melenk, I. Babuška, The partition of unity finite element method: Basic theory and applications, *Comput. Methods Appl. Mech. Eng.* 139 (1-4) (1996) 289–314.
- H. Li, J. Li, H. Yuan, A review of the extended finite element method on macrocrack and microcrack growth simulations, *Theor. Appl. Fract. Mech.* 97 (2018) 236–249.
- T. Belytschko, R. Gracie, G. Ventura, A review of extended/generalized finite element methods for material modeling, *Modell. Simul. Mater. Sci. Eng.* 17 (2009), 043001.
- Z. Wang, T. Yu, T.Q. Bui, S. Tanaka, C. Zhang, S. Hirose, J.L. Curiel-Sosa, 3-D local mesh refinement XFEM with variable-node hexahedron elements for extraction of stress intensity factors of straight and curved planar cracks, *Comput. Method. Appl. Mech.* 313 (2007) 375–405.
- J.P. Pereira, C.A. Duarte, X. Jiao, Three-dimensional crack growth with hp-generalized finite element and face offsetting methods, *Comput. Mech.* 46 (2010) 431–453.
- G. Xiao, L. Wen, R. Tian, Arbitrary 3D crack propagation with Improved XFEM: Accurate and efficient crack geometries, *Comput. Method. Appl. Mech.* 377 (2021) 113659, <https://doi.org/10.1016/j.cma.2020.113659>.
- F.M. Mukhtar, P.D. Alves, C.A. Duarte, Validation of a 3-D adaptive stable generalized/eXtended finite element method for mixed-mode brittle fracture propagation, *Int. J. Fract.* 225 (2020) 129–152.
- A.R. Khoei, *Extended Finite Element Method: Theory and Applications*, John Wiley & Sons, London, 2014.
- T.P. Fries, A corrected XFEM approximation without problems in blending elements, *Int. J. Numer. Methods Eng.* 75 (2008) 503–532.
- E. Béchet, H. Minnebo, N. Moës, B. Burgardt, Improved implementation and robustness study of the X-FEM for stress analysis around cracks, *Int. J. Numer. Methods Eng.* 64 (2005) 1033–1056.
- K. Agathos, E. Chatzi, S.P.A. Bordas, Stable 3D extended finite elements with higher order enrichment for accurate non planar fracture, *Comput. Method. Appl. Mech.* 306 (2016) 19–46.
- R. Tian, L. Wen, L. Wang, Three-dimensional improved XFEM (IXFEM) for static crack problems, *Comput. Method. Appl. Mech.* 343 (2019) 339–367.

- [56] V.F. González-Albuixech, E. Giner, J.E. Tarancón, F.J. Fuenmayor, Domain integral formulation for 3-d curved and non-planar cracks with the extended finite element method, *Comput. Method. Appl. Mech.* 264 (2013) 129–144.
- [57] Z. Cong, Y. Li, Y. Liu, Y. Xiao, A new method for calculating the direction of fracture propagation by stress numerical search based on the displacement discontinuity method, *Comput. Geotech.* 140 (2021), 104482.
- [58] P. Dumstorff, G. Meschke, Crack propagation criteria in the framework of X-FEM-based structural analyses, *Int. J. Numer. Anal. Methods Geomech.* 31 (2007) 239–259.
- [59] E.W. Remij, J.J.C. Remmers, F. Pizzocolo, D.M.J. Smeulders, J.M. Huyghe, A partition of unity-based model for crack nucleation and propagation in porous media, including orthotropic materials, *Transp. Porous Media* 106 (3) (2015) 505–522.
- [60] B. Mittelman, Z. Yosibash, Energy release rate cannot predict crack initiation orientation in domains with a sharp V-notch under mode III loading, *Eng. Fract. Mech.* 141 (2015) 230–241.
- [61] Z. Yosibash, B. Mittelman, A 3-D failure initiation criterion from a sharp V-notch edge in elastic brittle structures, *Eur. J. Mech. A. Solids* 60 (2016) 70–94.
- [62] G.N. Wells, L.J. Sluys, A new method for modelling cohesive cracks using finite elements, *Int. J. Numer. Methods Eng.* 50 (2001) 2667–2682.
- [63] C. Meng, D.D. Pollard, Modeling mixed-mode fracture propagation in 3D, in: 46th U.S. Rock Mechanics/Geomechanics Symposium, American Rock Mechanics Association, Chicago, Illinois, 2012, pp. ARMA-2012-2179.
- [64] D.S.H. Lo, *Finite Element Mesh Generation*, CRC Press, New York, 2015.
- [65] L. Sun, G. Zhao, X. Ma, Adaptive generation and local refinement methods of three-dimensional hexahedral element mesh, *Finite Elem. Anal. Des.* 50 (2012) 184–200.
- [66] C.D. Boor, *A Practical Guide to Splines*, Springer-Verlag, New York, 2001.
- [67] S. Loehnert, D.S. Mueller-Hoeppe, P. Wriggers, 3D corrected XFEM approach and extension to finite deformation theory, *Int. J. Numer. Methods Eng.* 86 (2011) 431–452.
- [68] I.M. Smith, D.V. Griffiths, L. Margetts, *Programming the Finite Element Method*, Fifth, Edition ed., John Wiley & Sons, West Sussex, United Kingdom, 2014.
- [69] A.R. Khoei, M. Eghbalian, H. Moslemi, H. Azadi, Crack growth modeling via 3D automatic adaptive mesh refinement based on modified-SPR technique, *Appl. Math. Model.* 37 (2013) 357–383.
- [70] K. Agathos, E. Chatzi, S.P.A. Bordas, A unified enrichment approach addressing blending and conditioning issues in enriched finite elements, *Comput. Method. Appl. Mech.* 349 (2019) 673–700.
- [71] P.A. Wawrzynek, B.J. Carter, C.-Y. Hwang, A.R. Ingraffea, Advances in simulation of arbitrary 3D crack growth using FRANC3D/NG, *J. Comput. Struct. Eng. Instit. Korea* 23 (2010) 607–613.
- [72] G. Ferté, P. Massin, N. Moës, 3D crack propagation with cohesive elements in the extended finite element method, *Comput. Method. Appl. Mech.* 300 (2016) 347–374.
- [73] R. Citarella, F.-G. Buchholz, Comparison of crack growth simulation by DBEM and FEM for SEN-specimens undergoing torsion or bending loading, *Eng. Fract. Mech.* 75 (2008) 489–509.
- [74] M. Duflot, A meshless method with enriched weight functions for three-dimensional crack propagation, *Int. J. Numer. Methods Eng.* 65 (2006) 1970–2006.
- [75] J.E. Mark, *Polymer Data Handbook*, 2ed ed., Oxford University Press, New York, USA, 2009.
- [76] A.A. Savitski, E. Detournay, Propagation of a penny-shaped fluid-driven fracture in an impermeable rock: asymptotic solutions, *Int. J. Solids Struct.* 39 (26) (2002) 6311–6337.
- [77] H. Tada, P.C. Paris, G.R. Irwin, *Stress Analysis of Cracks Handbook*, 3<sup>rd</sup> ed., ASME Press, New York, 2000.
- [78] W.H. Press, S.A. Teukolsky, W.T. Vetterling, B.P. Flannery, *Numerical Recipes in Fortran: The Art of Scientific Computing*, Cambridge University Press, New York, 1992.
- [79] H. Tang, S. Wang, R. Zhang, S. Li, L. Zhang, Y. Wu, Analysis of stress interference among multiple hydraulic fractures using a fully three-dimensional displacement discontinuity method, *J. Pet. Sci. Eng.* 179 (2019) 378–393.
- [80] F. Shi, X. Wang, C. Liu, H. Liu, H. Wu, A coupled extended finite element approach for modeling hydraulic fracturing in consideration of proppant, *J. Nat. Gas Sci. Eng.* 33 (2016) 885–897.